Photoreceptor loss does not recruit neutrophils despite strong microglial activation

Derek Power,[1,2] Justin Elstrott,[3] Jesse Schallek[1,2,4]

Corresponding author: Jesse Schallek, Flaum Eye Institute, University of Rochester, Rochester, NY 14642, USA

Email: jschall3@ur.rochester.edu

Phone number: +1-585-273-4848

[1]Center for Visual Science, University of Rochester, Rochester, NY 14627, USA

[2]Flaum Eye Institute, University of Rochester, Rochester, NY 14642, USA

[3]Department of Translational Imaging, Genentech Inc., South San Francisco, CA 94080, USA

[4]Department of Neuroscience, University of Rochester, Rochester, NY 14642, USA

Impact statement: Systemic neutrophils do not respond to laser-induced photoreceptor damage despite the robust response from resident microglia

Financial support: Research was supported by the National Eye Institute of the National Institutes of Health under Award No. R01 EY028293, and P30 EY001319. Work was also supported by a collaborative grant from Genentech Inc, a Career Development Award and Career Advancement Award (Schallek) and Unrestricted Grant to the University of Rochester Department of Ophthalmology from Research to Prevent Blindness, New York, New York and the Dana Foundation David Mahoney Neuroimaging Award (Schallek)

Conflict of Interest statement: Portions of this work were funded by a collaborative grant from Genentech, Inc. (Elstrott) to examine the extent to which immune cells could be studied in the deep retina using adaptive optics. Schallek also has six patents held through the University of Rochester on adaptive optics technology.

Data availability statement: All data collected (~3 TB) is archived at the University of Rochester and is available upon request.

Abstract:

In response to central nervous system (CNS) injury, tissue resident immune cells such as microglia and circulating systemic neutrophils are often first responders. The degree to which these cells interact in response to CNS damage is poorly understood, and even less so, in the neural retina which poses a challenge for high resolution imaging in vivo. In this study, we deploy fluorescence adaptive optics scanning light ophthalmoscopy (AOSLO) to study fluorescent microglia and neutrophils in mice. We simultaneously track immune cell dynamics using label-free phase-contrast AOSLO at micron-level resolution. Retinal lesions were induced with 488 nm light focused onto photoreceptor (PR) outer segments. These lesions focally ablated PRs, with minimal collateral damage to cells above and below the plane of focus. We used in vivo (AOSLO, SLO and OCT) imaging to reveal the natural history of the microglial and neutrophil response from minutes-to-months after injury. While microglia showed dynamic and progressive immune response with cells migrating into the injury locus within 1-day after injury, neutrophils were not recruited despite close proximity to vessels carrying neutrophils only microns away. Post-mortem confocal microscopy confirmed in vivo findings. This work illustrates that microglial activation does not recruit neutrophils in response to acute, focal loss of PRs, a condition encountered in many retinal diseases.

Introduction

In the mammalian retina, a rapid and coordinated immune response to infection or injury is important for maintaining tissue homeostasis. This is especially critical in the eye since mature retinal neurons do not typically regenerate, resulting in long-term functional losses for the host.[1,2] The retina is considered immune-

privileged and is equipped with a resident population of innate immune cells including microglia.[3,4] In healthy retina, microglia are distributed primarily in the inner retina, residing within nerve fiber layer (NFL), inner plexiform layer (IPL) and outer plexiform layers (OPL).[5,6], generally avoiding the nuclear layers. Microglia tile the retina and like their counterparts in the brain, exhibit long, thin processes that continually probe the neuro-glial microenvironment.[4,7,8]

In addition to phagocytosing debris[9,10], regulating synaptic maintenance[11,12] and removing dead tissue[13,14], microglia can secrete chemokines to recruit other leukocytes to help fight infection and repair damaged tissue.[4,15–17] For many injuries, one of the first systemic responders recruited and activated by microglia are neutrophils.[18,19] Neutrophils comprise a large fraction of leukocytes in murine blood (7.4 – 33.9%, “young” C57BL/6J mice[20]). They assist in maintaining tissue homeostasis by neutralizing foreign agents, regulating the immune response, and phagocytosing dead tissue[21,22]. Under inflammatory conditions, the spatiotemporal interplay between microglia and neutrophils is poorly understood. A missed window of interaction is highly problematic in histological study where a single time point reveals a snapshot of the temporally complex immune response, which changes dynamically over time. Here, we use in vivo imaging to overcome these constraints.

Documenting immune cell interactions in the retina over time has been challenged by insufficient resolution and contrast to visualize single cells in the living eye. The microscopic size of immune cells requires exceptional resolution

for detection. Recently, advances in AOSLO imaging have provided micron-level resolution and enhanced contrast for imaging individual immune cells in the retina and without requiring extrinsic dyes[7,23]. AOSLO provides multi-modal information from confocal reflectance, phase-contrast and fluorescence modalities, which can reveal a variety of cell types simultaneously in the living eye. Here, we used confocal AOSLO to track changes in reflectance at cellular scale. Phase-contrast AOSLO provides detail on highly translucent retinal structures such as vascular wall, single blood cells[27–29], PR somata[30], and is well-suited to image resident and systemic immune cells.[7,23] Fluorescence AOSLO provides the ability to study fluorescently-labeled cells[25,31,32] and exogenous dyes[27,33] throughout the living retina. These modalities used in combination have recently provided detailed images of the retinal response to a model of human uveitis.[23,34] Together, these innovations now provide a platform to visualize, for the first time, the dynamic interplay between many immune cell types, each with a unique role in tissue inflammation. We combine these innovative modalities with conventional histology as well as commercial OCT to reveal the progressive nature of the cellular response to acute retinal injury.

Here, we ask the question: “To what extent do microglia/neutrophils respond to acute neural loss in the retina?” To begin unraveling the complexities in this response, we deploy a deep retinal laser ablation model. Using AOSLO, we track and characterize the changes in microglia, neutrophils and retinal structure within hours, days and months after acute laser exposure.

Methods:

Key Resources Table				
Reagent type (species) or resource	**Designation**	**Source or reference**	**Identifiers**	**Additional information**
strain, strain background (*Mus musculus*)	C57BL/6J	The Jackson Laboratory	Strain #: 000664	
strain, strain background (*Mus musculus*)	CX3CR1-GFP	The Jackson Laboratory	Strain #: 005582	
strain, strain background (*Mus musculus*)	Catchup	Laboratory of M. Gunzer	C57BL/6-*Ly6g*(tm2621(CretdTomato) Arte	(Hasenberg *et al*. 2015) [35]
antibody	Ly-6G-647	Biolegend	Cat #: 127610 RRID:AB_1134159	IF (1:200)
other	DAPI stain	Cell Signaling Technology	Cat #: 4083	1:500 of 10 mg/ml stock
chemical compound, drug	Lipopolysaccharide (LPS)	Sigma-Aldrich	Cat #: L4391	1 ng (1 µl) delivered intravitreally

software, algorithm	Cell counter plugin	Imagej FIJI	Cell counter plugin	Author: Kurt De Vos, Imagej version 1.53q

Mice

All experiments herein were approved by the University Committee on Animal Resources (protocol #: UCAR-2010-052E) and according to the Association for Research in Vision and Ophthalmology statement for the Use of Animals in Ophthalmic and Vision Research as well as institutional approvals by the University of Rochester. C57BL/6J (#000664, Jackson Labs, Bar Harbor, ME) mice were used to track the retinal phenotype after laser exposure. Heterozygous CX3CR1-GFP (#005582, Jackson Labs) mice were used to track GFP-expressing microglia. Mice with heterozygous transgenic expression of tdTomato in neutrophils ("Catchup" mice) were provided by the foundry lab of M. Gunzer.[35] 18 mice (10 male, 8 female) in total were used for *in vivo* imaging. 10 additional mice (5 male, 5 female) were used for *ex vivo* histology. Age for all mice used for this work were post-natal weeks 6 - 24.

Preparation for *in vivo* imaging

Mice were anesthetized with intra-perotineal injection of ketamine (100 mg/kg) and xylazine (10 mg/kg). The pupil was dilated with 1% tropicamide (Sandoz, Basel, Switzerland) and 2.5% phenylephrine (Akorn, Lake Forest, IL). A custom

contact lens (1.5 mm base curve, 3.2 mm diameter, +10 diopter power, Advanced Vision Technologies, Lakewood, CO) was fitted to the eye. For a subset of experiments, 50 mg/kg fluorescein (AK-FLUOR, Akorn, Decatur, IL) was administered by intra-peritoneal injection to confirm vascular integrity and perfusion status after injury. During AOSLO imaging, anesthesia was supplemented with 1% (v/v) isoflurane in oxygen and mice were maintained at 37°C via electric heat pad. Eye hydration was maintained throughout imaging with regular application of saline eye drops (Refresh tears, Allergan, Sydney, Australia) and lubricating eye gel (Genteal, Alcon Laboratories Inc. Fort Worth, TX). Mice were placed in a positioning frame with 6-degrees of freedom to allow for stable animal positioning and aid in retinal navigation relative to the beam of the AOSLO and OCT.

In vivo **AOSLO imaging**

Four light sources were used for AOSLO imaging. A 904 nm diode source (12 µW, Qphotonics, Ann Harbor, MI) was used for wavefront sensing. A second 796 nm superluminescent diode (196 µW, Superlum, Cork, Ireland) was used for reflectance imaging, including confocal and phase contrast modes.[27,31] A third 488 nm light source (56 µW, Toptica Photonics, Farmington, NY) was used to visualize GFP-positive microglia in CX3CR1-GFP mice. A fourth 561 nm light source (95 µW, Toptica Photonics) was used to visualize tdTomato-positive neutrophils in Catchup mice. All light sources were fiber-coupled and axially

combined through the AOSLO system[31]. Fast (15.4 kHz) and slow (25 Hz) scanners create a raster scan pattern, which is relayed through a series of afocal telescopes to and from the eye. A Shack-Hartmann wavefront sensor (consisting of a lenslet array and a Rolera XR camera, QImaging, Surrey, Canada) measures the aberrations of the eye and a deformable mirror (ALPAO, Montbonnot-Saint-Martin, France) provided the wavefront correction. Reflected 796 nm light was collected with a photomultiplier tube (H7422-50, Hamamatsu Photonics, Hamamatsu, Japan). All confocal reflectance images were captured with a 30 µm pinhole (1.3 Airy Disc Diameters, ADD). Phase-contrast was achieved by displacing the pinhole relative to the principal axis of the detection plane as previously described.[25] Fluorescence was captured with a photomultiplier tube (H7422-40, Hamamatsu) either coupled with a 520Δ35 band-pass filter (FF01-520/35-25, Semrock, Rochester, NY) for GFP emission, or a 630Δ92 band-pass filter (FF01-630/92-25, Semrock) for tdTomato emission. All fluorescent images were captured with a confocal 50 µm pinhole (2.1 ADD). Image field sizes were either 4.98° x 3.95° or 2.39° x 1.94°. NIR and visible imaging channels were made coplanar, compensating for longitudinal chromatic aberration by independently focusing each light source onto the same axial structure in the retina. Through-focus stacks were acquired by sequentially changing the focus from NFL to the PR outer segments by using the defocus term on the custom adaptive optics control software.

As described previously, red blood cell (RBC) imaging was achieved by combining phase-contrast imaging with a strategy to arrest the slow galvanometer scanner and let the resonant scanner project a single “line” (0.71° scan angle) on the retina. This enabled RBC flux imaging by positioning this line orthogonal to the direction of flow for single capillaries. As blood cells moved through capillaries, they were “self-scanned” producing images of RBCs in space/time[27].

PR laser damage model and post-injury time points for imaging

488 nm light (Continuous wave Laser diode, ±4 nm bandwidth, Toptica Photonics) was used to create an acute laser injury. 785 µW of 488 nm light was projected through the AOSLO and focused onto the PR outer segments (Figure 1a) for 3 minutes in a single line on the retina subtending 24 x 1 µm to concentrate the power to a small region. Laser injuries were placed between 5-15° from the optic disc. To avoid absorption confounds, we refrained from placing lesions beneath large retinal vessels. For experiments examining neutrophil involvement, lesions were placed <100 µm away from retinal veins and within microns of capillaries to increase the chance of extravasation through these preferred pathways in the retina[36–38]. As many as four such lesions were placed per retina. This protocol produced a hyper-reflective phenotype in the >40 locations across 28 mice. In rare cases, the exposure yielded no hyper-reflective lesion and were often in mice with high retinal motion, where the light dosage

was spread over a larger retinal area. These locations were not included in the in-vivo or histological analysis.

Throughout this work, we assessed the effects of the laser injury for the following time points: baseline/control, 1 day (defined as 18 – 28 hours post-damage), 3 days, 7 days and 2 months.

In vivo SLO, and OCT imaging

To confirm global ocular health and changes imparted by the laser damage, a commercial Heidelberg Spectralis system (Heidelberg, Germany) was used to acquire scanning laser ophthalmoscopy (SLO) and optical coherence tomography (OCT) images. 30° and 55° fields were used for SLO acquisitions. The 30° field was used for OCT acquisitions. For some experiments, fluorescein angiography was captured by imaging the retina within 10 minutes of fluorescein administration (details above). The fluorescence mode of the SLO also enabled wide-field images of GFP positive microglia.

OCT was acquired with the following settings: ART 16 (automatic real-time tracking) was used to average B-scans and improve signal. To capture several damage locations in a single field, we used a coarse scan area (61 B-scans, 1.02 x 0.85 mm). A dense 3D data cube was also captured (49 B-scans, 513 x 171 µm) to provide detailed information regarding the axial nature of the laser damage. “Follow-up” mode, which allows the HRA software to return to the same retinal location, was used whenever possible. To reveal the cross-sectional

profile for each lesion, several adjacent B-scans were spatially averaged (~30 μm).

Preparation for *ex vivo* imaging

Mice were euthanized by CO_2 asphyxiation followed by cervical dislocation. Within 5 minutes of asphyxiation, eyes were enucleated and placed in 4% paraformaldehyde (PFA, diluted from: #15714-S, Electron Microscopy Sciences, Hatfield, Pennsylvania) in 1x phosphate buffered saline (PBS, #806552, Sigma-Aldrich, St. Louis, MO) for one hour at room temperature. Eyes were dissected to remove the cornea, lens and vitreous. Each eye cup was placed in one well of a 24-well plate containing 0.5 ml of 0.8% PFA and left overnight at 4°C. The retina was separated from the retinal pigmented epithelium/choroid with attention to preserve inner retinal layers “up” orientation. If not applying antibody, the tissue was directly flat mounted (see below). For antibody staining, the retina was placed in 1x BD perm/wash buffer (#554723, BD Biosciences, Franklin Lakes, NJ) with 5% donkey serum (#D9663, Sigma-Aldrich) diluted in PBS for overnight incubation at room temperature with gentle shaking. The following was performed in the dark. Ly-6G-647 antibody (1:200, #127610, RRID:AB_1134159, BioLegend, San Diego, CA) and DAPI (1:500 of 10 mg/ml stock, #4083, Cell Signaling Technology, Danvers, MA) were diluted in 1x perm/wash buffer and retinas were incubated for 3 days at room temperature with gentle shaking. Retinas were washed with PBS three times over three hours. The retina was cut into 4 radially symmetrical petals, flat-mounted on a glass slide in Vectashield

mounting buffer (H-1000-10, Vector labs, Newark, CA) with a #1.5 cover slip (#260406, Ted Pella Inc., Redding, CA), sealed with nail polish and stored at 4°C until imaged.

Endotoxin-Induced Uveitis protocol

To serve as a positive control and show evidence of known neutrophil invasion, we adopted the endotoxin-induced uveitis (EIU) model to confirm that fluorescent Catchup neutrophils could be observed in vivo with AOSLO. This was performed in two mice. The EIU model has been described previously.[34,39] Briefly, we performed intravitreal injections of lipopolysaccharide (LPS, #L4391, Sigma-Aldrich). Mice were anesthetized with ketamine and xylazine. A 34 gauge Hamilton needle was used to deliver 1 µL (1 ng) of LPS diluted in PBS into the vitreous posterior to the limbus. 1 day post-LPS injection, mice were either imaged with AOSLO (Catchup mice) or collected for *ex vivo* histology (Ly-6G-647 stained C57BL/6J mice) to confirm fluorescent neutrophil presence in the neural parenchyma.

***Ex vivo* confocal imaging**

Whole-mount retinas were imaged with a Nikon A1 confocal microscope (Melville, NY). DAPI (405 nm ex, 441Δ66 nm em), CX3CR1-GFP (488 nm ex, 525Δ50 nm em), and Catchup/anti-Ly-6G-647 (635 nm ex, 665Δ50 nm em) were simultaneously imaged. Z-stacks (0.1 or 0.5 µm step size) at control or laser-damaged locations were acquired with a 60x oil objective, producing images that

were 295 x 295 µm. Larger (796 x 796 µm) z-stacks were acquired by blending several 60x z-stack acquisitions (3x3, 15% overlap) using Nikon NIS Elements software. z-stacks were re-sliced (Imagej FIJI[42], X-Z dimension) to visualize fluorescence depth profiles.

AOSLO image processing

To correct residual motion from heart rate and respiration, AOSLO videos were registered with a custom cross-correlation-based frame registration software.[40,41] Motion correction was also applied to simultaneously collected fluorescence videos. After registration, confocal, phase-contrast and fluorescence AOSLO videos were temporally averaged (250 frames, 10 seconds). Blood perfusion maps were computed by calculating the standard deviation of pixel intensity over 30 seconds[32].

INL + ONL nuclei quantification

Raw DAPI z-stacks were used for manual counting of nuclei (n = 10 mice, 3 regions per time point). Analysis regions were circular, with a 50 µm diameter (corresponding to the size and shape of the damage region seen with confocal AOSLO) and analyzed in depth producing volumetric cylinders through the INL or outer nuclear layer (ONL, Figure 3d,e). Nuclei were counted manually using the "Cell Counter" plugin in Imagej (Author: Kurt De Vos, Imagej version 1.53q).

PR + Microglia nuclei volume quantification

A single DAPI-stained z-stack (OPL + ONL) from a CX3CR1-GFP mouse was used to quantify nuclear volume of PR's (n = 20) and microglia (n = 14). Data was centered at a lesion location 3 days post-laser exposure. Imagej was used to manually measure the en-face diameter of nuclei in their short and long axis. We averaged the two measurements and assumed spherical shape for analysis. These measurements aided in the differentiation of PR's, invading microglia and PR phagosomes.

Quantification of RBC flux in capillaries

Using the capillary line-scan approach[27,43,44], we quantified RBC flux within an epoch of 1 second. This spanned several cardiac cycles.[29,45] To improve SNR, space-time images were convolved with a Gaussian spatio-temporal filter (σ = 7.5 pixels, 0.33 μm). This strategy did not interfere with spatial resolution as pixels oversample the optical point-spread of the AOSLO by >20x.[27] RBC flux was determined by manually marking blood cells using the "Cell counter" plugin in Imagej.

Neutrophil density quantification

Ly-6G-647-stained retinal tissue was used to manually count neutrophils within montaged 796 x 796 μm z-stacks. Cells were counted at control (n = 4 locations, 2 mice) and lesioned (n = 4 locations, 2 mice) locations using the "Cell Counter" Imagej plugin. All values are reported as mean ± SD. There were no data points omitted from any of the analysis reported in this work.

Results:

Characterization of deep focal laser damage

Four complementary imaging modalities were used to evaluate the nature and localization of the focal laser damage induced by 488 nm light: wide field SLO, OCT, AOSLO and post-mortem histology. Each is reported in turn below.

Laser damage induces focal hyperreflective lesions in outer retina imaged with wide-field SLO

To observe global and focal retinal health, we used commercial SLO. 1 day post-488 nm light exposure, both NIR and blue reflectance modalities showed hyperreflective lesions, most apparent at a deeper retinal focus position. When SLO focus was brought to the inner retina, lesions were not visible and retina appeared healthy (Figure 1b). Despite deep retinal damage, fluorescein angiography did not reveal dye leakage (Figure 1b, bottom), indicating the blood retinal barrier remained intact.

OCT B-scans reveal outer retinal hyperreflection without inner retinal damage

To assist in determination of which retinal layers are damaged by the 488 nm laser, we used OCT. Within 30 minutes post-laser exposure, OCT revealed a zone of hyperreflection within the ONL (Figure 1 – figure supplement 1). 1 day post-lesion, the focal hyperreflection remained localized to the ONL (~50 µm

wide, Figure 1c). Retina outside of damage foci appeared normal. The hyperreflective phenotype persisted through 7 days and was cleared by 2 months (Figure 2a). There did not appear to be any cellular excavation, “cratering” or evidence of edema for any time point assessed. Despite the hyperreflective ONL phenotype, Bruch’s membrane appeared intact for all time points, evidenced by lack of fluorescein leakage at the site of lesion. Additionally, retinal vessels appeared normal in OCT B-scans.

AOSLO reveals outer retinal damage with confocal and phase-contrast modalities

Confocal AOSLO provided micron-level detail of the lesioned area. Confirming OCT findings, we observed hyperreflective changes localized within the ONL that were, by 1 day, the brightest at the OPL/ONL interface (Figure 2b). At this plane, the lesions manifest as an ellipse with the long axis in the direction of the line scan used to create the lesion. The most prominent hyperreflective phenotype was seen at 1 day post lesion, with diminishing size and brightness by day 3 and 7. The phenotype was largely diminished by 2 months (Figure 2b).

Using phase-contrast AOSLO also allowed visualization of translucent cells within the retina which enabled us to image PR somas of the ONL[25,30]. Normally, the ONL is comprised of PR somata that are densely-packed[30,46]. We found that the dense packing of individual somata was disrupted 1 day post-

exposure (~50 µm ovoid, Figure 2c), suggesting degradation or ablation of the cell membrane.

Confirmation of outer retinal cell loss using post-mortem histology

To assess the extent of cell loss caused by focal laser exposure, we performed DAPI staining on whole-mount retinal tissue using the same time points assessed for *in vivo* imaging. 1 day after laser exposure, we observed mild thickening of the ONL compared to unexposed locations only microns away. At 3 and 7 days, local ONL thinning was observed (Figure 3a). En-face planes within the ONL revealed a loss of PR nuclei in the outer aspect of the ONL for 3 and 7 day time points, while inner ONL exhibited little evidence of cell loss (Figure 3b, c), illustrating the precise axial confinement of the laser damage induced by this method. By 2 months, the lesion's overall appearance and ONL thickness returned to baseline (Figure 3a-c). This histological finding corroborates the OCT findings observed *in vivo*.

ONL nuclear counts were reduced at locations of laser exposure. In comparison to control locations (501317 nuclei/mm^2 ± 46198 nuclei/mm^2, mean ±SD, similar to previous work[47]), at 3 and 7 days post-exposure, we found a corresponding reduction in the density of ONL nuclei of 18% (408965 nuclei/mm^2 ± 25621 nuclei/mm^2) and 27% (367542 nuclei/mm^2 ± 9038 nuclei/mm^2) respectively. Compared to control locations, the 3 and 7 day data resulted in p-values of 0.17 and 0.07, respectively (Student's paired two-tailed t-test). 2

months after damage, PR nuclear densities were indistinguishable from that of control (Figure 3f, gray bars). Despite losses of PR nuclei, total cell nuclei within the INL remained unchanged for all time points (Figure 3f, black bars). These data indicate that the laser exposure focally ablated PR's whilst leaving inner retinal cells intact.

Retinal vasculature unaffected by deep retinal lesion

A concern with laser lesions of this type is that it may coagulate retinal vessels. Motion contrast[26,27] images revealed that the vasculature remained perfused from hours to months after laser damage suggesting that acute or long term changes are not imparted by the laser injury (Figure 4). None of the primary vascular stratifications within the NFL, IPL and OPL of the mouse retina[32] showed stopped flow as a result of the laser lesion, reinforcing the findings above regarding the axial confinement of the damage to the outer retina.

In addition to perfusion status, phase-contrast AOSLO also permitted analysis of single blood cell flux within capillaries[27,48]. We tracked capillary flux at different retinal depths within and above the lesion (IPL, OPL, 1 capillary each, Figure 4 – figure supplement 1a). Blood cell flux for capillaries within lesion locations were within the range of normal flux for the C57BL/6J mouse[48] (Figure 4 – figure supplement 1b, c). Flux tracked from hours to days in these capillaries changed synchronously, displaying positive linear correlation (R^2 = 0.59, Figure 4 – figure supplement 1c, d). This suggested any such changes in flux were a

property of systemic perfusion, rather than locally imparted changes in flow due to the lesion. As an additional control, we evaluated blood flux in two distant capillaries (control, Figure 4 – figure supplement 1e). Both capillaries displayed similar flux values from minutes to 2 months post-injury (Figure 4 – figure supplement 1f, g) resulting in positive linear correlation (R^2 = 0.78, Figure 4 – figure supplement 1h). Taken together, these findings suggest lesions do not appreciably impact local RBC delivery in the capillary network.

PR laser injury promotes a robust response in nearby microglia

To observe the microglial response to PR laser injury, we imaged fluorescent microglia in CX3CR1-GFP mice with both SLO and AOSLO. 1 day after injury, SLO revealed bright, focal congregations of microglia at injury locations in contrast to undamaged locations, which maintained a distribution of lateral tiling (Figure 5a, b). The global visualization of microglia was augmented by high resolution fluorescence AOSLO, providing enhanced detail of the microglial response to laser injury[7,49]. Whereas AOSLO imaging of microglia in the healthy retina displayed a distributed array of microglia with ramified processes (Figure 5c, left), laser damaged locations showed a congregation of cells 1 day post-injury with less lateral ramification (Figure 5c, right). Within hours of the laser exposure, we did not observe a photo-bleaching or death of regional microglia suggesting that while the laser exposure was sufficient to damage PR's, it left retinal microglia intact.

With phase-contrast imaging targeting the ONL, we documented a rare event of putative pseudopod extension at a lesion site (Figure 5 – video 1). Given the axial complexity of microglia in this layer, it is now possible that microglial process dynamics may be revealed with this label-free approach.

We returned to the same laser-damaged locations to capture microglial appearance at baseline, 1, 3, 7 day and 2 month time points with AOSLO to track the natural history of the microglial response to PR damage. At 1 day post-injury, damage locations displayed aggregations of microglia. The surrounding microglia displayed process polarization with extensions projecting toward the injury (Figure 6). By days 3 and 7, microglia exhibited fewer lateral projections and somas have migrated into the ONL where they do not normally reside (Figure 6). By 2 months post-injury, the hyperreflective phenotype was absent and microglia once again occupied only the inner retina. The microglial distribution at 2 months was similar to baseline, with cells exhibiting radially symmetrical branching projections, similar to those prior to laser injury (Figure 6).

A standing question in OCT/confocal AOSLO lesion interpretation is whether microglia contribute or directly produce the hyperreflective phenotype seen in axial B-scans and en-face fundus images[50,51]. With confocal AOSLO, we find that the hyperreflective phenotype is visible as early as 30 minutes, becoming larger and brighter by 90 minutes. During these time points, simultaneously imaged microglia remained ramified and maintained a tiled

arrangement, indicating that microglial are not the initial source of the lesion-induced hyperreflective appearance (Figure 6 – figure supplement 1).

Despite robust microglial involvement, neutrophils do not extravasate

While we observed a robust microglial response to PR damage, there was no evidence of neutrophil involvement at the times we examined (1, 3, 7 day, and 2 month follow-up).

In vivo fluorescence imaging allowed us to track neutrophils with AOSLO in Catchup mice[35]. In healthy mice, we observed a sparse population of circulating neutrophils flowing quickly within the largest retinal vessels (Figure 7 – video 1). We also observed neutrophils moving through single capillary branches (Figure 7 – video 2). We found that neutrophils show deformation within the small confines of the capillary lumen, often resulting in tube or pill-shaped morphology seen both in vivo and ex vivo (Figure 7b, top).

After laser lesion, we found no evidence of neutrophil aggregation or extravasation for any time point assessed (Figure 8). There was also a notable lack of rolling/crawling neutrophils (or any putative leukocyte) in large arterioles or venules surrounding the injury (Figure 8 – video 1). Neutrophils closest to the ONL lesion were occasionally detected within the deepest retinal capillaries. However, these neutrophils stayed within the retinal vasculature, as evidenced by their pill-shaped morphology and passage routes that follow the known vascular paths seen in confocal/phase contrast images (Figure 8 – video 2).

Leukocytes, including neutrophils, often impede flow due to their large size (13.7 µm[52]) as they compress through capillaries <7 µm in diameter[48]. However, we found no evidence of permanently stopped flow, as rare stalls would re-perfuse similar to those previously characterized in healthy mice (Figure 7a).[48]

As a positive control, we used the EIU model in Catchup mice to show that we could image extravasated neutrophils. This model is known to induce a strong neutrophil response. With fluorescence AOSLO, we found Catchup-positive neutrophils within the retinal parenchyma, providing confirmation that extravasated neutrophils can be imaged with this modality. Moreover, we found that neutrophils that have extravasated into the retinal parenchyma tended to have a more spherical morphology rather than the compressed, pill-shaped morphology of neutrophils within capillaries (Figure 7b).

Ex vivo **analysis confirms** ***in vivo*** **findings**

To confirm our *in vivo* findings, we examined fluorescent microglia and neutrophils in laser-damaged retinal whole-mounts imaged with confocal microscopy. The progressive nature of the microglial response to PR damage and general lack of neutrophil participation corroborated *in vivo* findings.

Ex vivo**: Microglia display dynamic morphological changes in lesion areas**

Without laser damage, microglia exhibited a tiled distribution and stellate morphology with highly-ramified branching patterns (Figure 9a). 1 day after laser exposure, microglial somas aggregated to the lesion location. They began to

migrate into the ONL and changed from the ramified, and pancake-flat morphology seen in the healthy retina, to a dagger-like axial morphology (figure 9b). At 3 and 7 days after lesion, microglia migrated deeper into the outer retina and remained aggregated with an axially elongated phenotype. 2 months after lesion, microglial somas were no longer found in the ONL. Instead, microglia redistributed similar to that of the healthy retina, once again co-stratifying predominantly with the NFL and plexiform layers of the retina (Figure 9a, b, Video 1).

Whereas we found a robust response of deep microglia at the OPL to PR injury, we observed little migratory response of the microglia in the NFL or IPL (Figure 9 + Figure 9 – figure supplement 1) suggesting axial and lateral constraints on the extent of microglial recruitment.

Microglia form PR-containing phagosomes

A detailed examination of microglial involvement with PR somata in response to PR injury revealed unique microglia-PR interactions within the ONL. In cross-section, PR cells comprise a large portion of the retina reaching from the outer-segment tip, inner segments, somata and spherule/pedicle synaptic contacts at the OPL. Likewise, we saw microglial involvement with all of these layers. Within 1 day, we found microglial processes interspersed within the dense aggregation of PR somata within the ONL. Amoeboid cells enveloped the somata of PR's and phagocytosis was detected 1, 3 and 7 days post-laser exposure (Figure 9 –

figure supplement 2). Confocal microscopy revealed GFP-positive processes surrounding PR nuclei, engulfing multiple somata (Figure 9 – figure supplement 2a, c). By 3 days, microglial processes and somas migrated deeper, with processes extending into the distal portions of the PR cells including the inner/outer segments. By two months microglial processes and somas had retreated out of the ONL.

DAPI nuclear stain combined with confocal microscopy not only helped us discern retinal neurons, but also allowed us to differentiate between microglia and phagocytosed PR's. Two features were different from PR and microglial nuclei. First, each PR displayed a uniform, homogeneous nuclear fluorescence, while microglial nuclei appeared heterogenous and mottled (Figure 9 - figure supplement 2a). Second, microglial nuclei were nearly 3x larger in volume compared to PR nuclei. Microglia had a nuclear volume of 110 ± 42 μm^3 and PR nuclei were 35 ± 5 μm^3 ($p < 0.001$, Figure 9 – figure supplement 2b). PR nuclei within microglial phagosomes displayed similar nuclear volume compared to adjacent PR's in undamaged locations (Figure 9 – figure supplement 2a).

***Ex vivo*: At lesion sites, neutrophils remain within the retinal vasculature**

Corroborating in vivo AOSLO findings we did not find neutrophil aggregation or extravasation in response to laser damage at any of the time points examined. *Ex vivo* microscopy revealed that neutrophils were found within the vascular network and did not extravasate into the neural retina. Very few neutrophils were

found in lesioned retinas, comparable healthy retinas. The few detected neutrophils were remnants of those found within the vascular network at point of death. Detailed 60x Z-stacks revealed “pill-shaped” morphology similar to that seen *in vivo*, where neutrophils are compressed within capillaries. This morphology contrasts with the spherical shape of neutrophils in response to the EIU positive-control model (Video 2). In one exceptional example (1 day post-damage), we observed two neutrophils in a single z-stack, one in a capillary (1) and one at a capillary branch point (2), but none were observed to have left the confines of the vasculature suggesting they were not recruited by activated microglia (Figure 9c,d, Video 2).

Retinal neutrophil concentrations were quantified from larger z-stacks (796 x 796 μm, Figure 10a). Control locations (n = 2 mice, 4 z-stacks) had 15 ± 8 neutrophils per mm^2 of retina whereas lesioned locations (n = 2 mice, 4 z-stacks) had 23 ± 5 neutrophils per mm^2 of retina (Figure 10b). The difference between control and lesioned groups were not statistically significant ($p = 0.19$).

Finally, when we rendered confocal Z-stacks in cross-sectional view, we discovered that the few fluorescent neutrophils present were found colocalized within the tri-layered vascular stratifications of the mouse retina [32,53,54]. None were found in non-vascular layers. Taken together, all *ex vivo* data indicates that regardless of the robust phagocytic microglial response, neutrophils remain localized within vessels, suggesting that neutrophils do not extravasate or

aggregate in response to this laser lesion model. These data corroborate the in vivo findings.

Discussion:

Summary

In many retinal diseases, resident microglial populations are found to exhibit cross-talk with systemic immune cells[15,18]. The complex temporal dynamics between resident and systemic immune cells unfolds from seconds-to-months and has been poorly characterized due to lack of resolution, sufficient contrast and a non-destructive imaging approach that can track changes over time. Here, we overcome these limitations by using phase-contrast and fluorescent imaging with adaptive optics to visualize the interaction of multiple cell types. With this advanced imaging technology, we reveal the absence of neutrophil involvement in response to an acute injury, despite progressive changes in microglial activity and morphology. Here we discuss the implications of such findings in the context of retinal damage and more broadly, to retinal disease.

Focal retinal lesions for tracking the immune response

Seminal studies in the brain have used focal light exposure to induce targeted, acute microglial responses.[59,60] Since then, it has been a popular damage model. Focal lesions in the retina have been conducted in a number of popular animal models including mouse[61,62], macaque[63–65] and cats.[66,67] Laser damage is also clinically relevant as it is both experienced with accidental laser exposure[68,69] as

well as purposeful ablation used in photocoagulation and as a therapy for retinal ischemic disease, retinopathy of prematurity[70] and diabetic retinopathy[71]. Thus our results shed light toward the immune response that may be imparted due to phototoxic damage.

Light damage offers a number of advantages for creating acute damage in the retina. It offers placement precision that is better controlled than other acute and invasive methods, such as incision/poke injuries[55], retinal detachment[56] and chemical injury[57,58]. In the mouse, focal light dosage comes with greater axial confinement within the retina by nature of the high numerical aperture of the mouse eye[31] which imposes minimal collateral damage to layers above or below the plane of focus (Figure 1a). The damage took on an elliptical form, likely due to: 1) Eye motion from respiration and heart rate which spreads the light over a larger integrative area (rather than line). 2) The impact of focal light scatter. 3) A micron-thin line imparting damage on cells that are many microns across manifesting as an ellipse. The majority of light exposures produced lesions of this elliptical shape. In a few conditions, for the reasons described above, the exposure failed to produce a strong, focal damage phenotype. To improve lesion reproducibility, future experiments should control for subtle eye motion affecting light damage, especially for long exposures.

Titration of the 488 nm laser leads to mild retinal damage

While it is beyond the scope of this report to catalog the vast parameter space in which light may impose damage in the retina, it is noteworthy to discuss that the exposure intensity, subtended angle and duration of the light source we used delivered an intentionally mild damage to the retina. Using dosages too high would run the risk of collateral damage to the blood retinal barrier or Bruch's membrane[72] which could cause a choroidal neovascularization phenotype[73]. This would be undesirable for studying the native/systemic immune response as it could confound the traditional extravasation pathways of the inflammatory system[23,74]. Instead, we chose our laser exposure condition to impart a weak, but reproducible loss of PRs while minimizing damage to the cells above and below the plane of focus.

Progressive PR loss and morphology of the lesion tracked over time

The amount of light delivered did not immediately ablate PRs as peak cell loss wasn't observed until 3-7 days after laser exposure, suggesting a progressive damage phenotype of apoptosis or necroptotic death. Histology showed a ~27% reduction in PR nuclei 7 days post lesion. The total number of PR nuclei within the lesion location returned to values similar to baseline by 2 months, which was surprising given that PRs do not regenerate. Our interpretation is that adjacent PRs spill into the region of loss, similar to what several have described previously[63,75]. Corroborating the histological finding of mild cell loss, OCT shows no evidence of local edema, cavitation or excavation of the ONL after PR loss (Figure 2a). The return of the appearance, thickness and redistribution of cells

within the ablated location indicates that retinal remodeling occurs within 2 months. The concurrence of microglia in these outer retinal bands (where they are normally absent[76]) support the hypothesis that microglia localized to this region to facilitate a phagocytic injury response and perhaps contribute toward synaptic remodeling[11].

CX3CR1-GFP mice exhibit fluorescence not only in microglia

We recognize that the CX3CR1-GFP model can also label systemic cells such as monocytes/macrophages[77]. While it is possible these cells could infiltrate the retina in response to the lesion, we find it unlikely since there was no indication of the leukocyte extravasation cascade (rolling/crawling/stalled cells) within the nearest retinal vasculature. In addition to microglia, retinal perivascular macrophages and hyalocytes also exhibit GFP fluorescence and thus that these cells may also contribute toward damage resolution.

The hyperreflective phenotype does not arise from microglia or neutrophils

Light damage is known to create hyper-reflective bands in OCT imaging [64,78,79]. A common speculation is that the increased backscatter may arise from local inflammatory cells that activate or move into the damage location. In our data, confocal AOSLO and OCT revealed a hyperreflective band at the OPL and ONL after 488 nm light exposure (Figure 2a, b). We found that the hyperreflective bands appeared within 30 minutes after the laser injury, preceding any detectable microglial migration toward the damage location (Figure 2 – figure

supplement 1 and Figure 6 – figure supplement 1). We thus conclude that the initial hyperreflective phenotype is not caused by microglial cell activity or aggregation.

Direct activation of microglia from 488 nm light exposure was minimal

It is conceivable that 488 nm light used for either imaging (56 μW) or imparting damage (785 μW) might activate the GFP-containing microglia used here. However, several lines of evidence speak against this possibility. 1) We did not observe photobleaching of CX3CR1 positive cells in response to the damage, suggesting the fluorescence imaging light was insufficient to damage microglia. 2) For retinal injury, the focal plane was adjusted using the AOSLO, such that the dose was axially concentrated onto the outer retina. Thus, the light dosage received by microglia above was defocused and less than the targeted PR layer (Figure 1a). 3) Histology showed no evident necrotic/apoptotic microglial morphologies.

488 nm laser lesion does not photocoagulate or alter retinal circulation

Despite imparting damage to the PRs, the damage regime used here did not alter the perfusion of the retinal circulation. We show three independent measures that blood flow is uninterrupted, despite PR loss and activation of microglia. 1) Fluorescein angiography (Figure 1b, bottom) revealed an absence of vascular leakage. 2) AOSLO motion contrast vascular maps [24,27,32] displayed persistent blood perfusion inside vessels near laser lesion sites (Figure 4). 3)

Capillary line scans indicate that RBC flux was not modified at lesion locations and fell within the normal range[27,48] (Figure 4 – figure supplement 1). Altogether, these three lines of evidence indicate that the lesion did not compromise the blood-retinal barrier or impart perfusion changes within the retinal vasculature.

Resident microglia do not need systemic neutrophils for resolution of mild laser-damage

The CNS and retina, unlike other peripheral tissues, cannot suffer from excess inflammation as there may be dire functional consequences. Therefore it is possible that microglia protect against exorbitant inflammation by modulating the recruitment of systemic inflammatory cells.[4,15–17] Of these, neutrophils are often one of the first systemic responders. Despite their helpful roles in other tissues, neutrophils can secrete neurotoxic compounds that could present a danger to the CNS.[80] Given their conflicted role in the body, we ask the question: to what extent do neutrophils respond to acute neural loss in the retina? Retinal cells are lost with age[81] and disease[82] and yet, for the organism, visual perception must persist. There are limitations on how generalizable this mild damage to more severe damage or disease phenotypes, but this acute damage model can begin to provide clues about how immune cells interact in response to PR loss. In this laser lesion model, we ablate 27% of the PRs in a 50 μm region.

We find that microglia undergo a rapid and progressive response to this injury. We show evidence of PR phagocytosis (Figure 9 - figure supplement 2),

interaction with neighboring microglia (Figure 9 – figure supplement 1) and they are also axially positioned to facilitate retinal remodeling (Figure 9). Furthermore, throughout the temporal evolution of the microglial response, we find no evidence of neutrophil recruitment despite the damage being within 10s of microns from retinal vessels that carry them. At the onset of the neutrophil extravasation cascade, endothelial cells in the vicinity of inflamed tissue typically elevate the expression of adhesion molecules, facilitating the adherence and extravasation of circulating neutrophils.[83] Furthermore, neutrophils are dependent on priming events as prerequisite to further activation and engagement of their effector functions.[84,85] Based on our data, we suggest that although microglia show a strong and lasting activation, at no time point from seconds-to-months, are the damage-associated molecular patterns or chemotactic gradients strong enough to recruit neutrophils in response to this damage. This is evidenced in our data from two key observations: 1) We saw no examples of systemic leukocytes rolling in vessels adjacent to injury locations (Figure 8 – video 1). 2) Using fluorescence, we did not observe adherent or extravasated neutrophils adjacent to imparted PR loss (Figure 8). This may suggest that the region of insult is too small, or that activated microglia are not sufficient for recruiting neutrophils with damage of this magnitude. Perhaps a minimum threshold of neural damage must be met before neutrophils will respond. It is possible that resident microglia facilitate the necessary phagocytic and retinal remodeling response despite release of cytokines from damaged retinal cells that would normally recruit

systemic immune cells in peripheral tissues. Such a strategy would benefit the CNS.

Future work will explore whether there is a threshold magnitude of neuronal cell loss required for recruitment of systemic cells that is unique to the retina. Next studies will examine more severe or widespread injury regimes that provide stronger activating molecular signals and interact with a larger population of systemic cells.

Microglia may inhibit neutrophil activation

Microglia may be involved in a system that protects the CNS from propagating a larger systemic response, potentially exacerbating disease pathologies that would compromise overall CNS function. In another damage model[86], they report that tissue-resident macrophages may exhibit the capacity to cloak tissue micro-damage. This offers the possibility that resident immune cells, such as retinal microglia, can handle small insults without inducing a chemokine cascade that may invoke a larger systemic response that could further damage the precious retinal tissue.[87] Regardless of the mechanism, we find that despite a robust microglial activation that lasts for weeks, at no time point do they recruit neutrophils. The nuance of this interaction likely represents the fine balance that facilitates a helpful local response within the CNS that does not impart a widespread cytokine storm that may otherwise exacerbate retinal damage. Further work will explore whether microglia exhibit a cloaking response in the

retina, inhibiting neutrophil or other immune cell extravasation/chemotaxis toward lesion sites. We expect such work to be pivotal in understanding the balance that is broken or left unchecked in conditions of autoimmune disease and the umbrella of diseases that comprise the uveitic response, a direct threat to lifelong vision.[88]

Conclusion

Here, we have applied innovative *in vivo* imaging at the microscopic scale to reveal the cellular immune response to a retina in jeopardy. The dynamic environment of the retina includes a native population of resident microglia and systemic immune cells delivered through the vasculature. These two lines of defense work in concert in the mammalian body and are critical for maintaining retinal homeostasis. In this work we directly study the interaction between microglia and neutrophils, two major classes of immune cells that are implicated in inflammatory initiation, escalation, propagation and debris removal in response to acute geographical injury in the retina. Using cutting-edge retinal imaging modalities, we find that resident microglia become locally activated and regionally responsive to focal laser lesion. Cells migrate away from their stratified locations near plexiform layers of the retina and migrate toward the site of damage within hours to weeks after injury. However, systemic neutrophils, which are typically regarded as first-line responders to tissue damage, are not recruited to this damage despite neutrophils flowing within 10s of microns away from the location of damage (Figure 8 – video 2). Beyond the context of this specific finding, we

share this work with the excitement that AOSLO cellular level imaging may reveal the interaction of multiple immune cell types in the living retina. By using fluorophores associated with specific immune cell populations, the complex dynamics that orchestrate the immune response may be examined in this specialized tissue. This work and future studies may reveal further insights to the interactions of single immune cells in the living body in a non-invasive way.

Acknowledgements: Thanks to Colin Chu**,** Justin Elstrott and Tiffany Heaster for useful intellectual conversations. Thanks to Minsoo Kim for generously transferring the Catchup mouse strain.

References:

1. Stone, J. *et al.* Mechanisms of photoreceptor death and survival in mammalian retina. *Progress in Retinal and Eye Research* **18**, 689–735 (1999).
2. García-Ayuso, D., Di Pierdomenico, J., Vidal-Sanz, M. & Villegas-Pérez, M. P. Retinal Ganglion Cell Death as a Late Remodeling Effect of Photoreceptor Degeneration. *Int J Mol Sci* **20**, 4649 (2019).
3. Boycott, B. B. & Hopkins, J. M. Microglia in the retina of monkey and other mammals: its distinction from other types of glia and horizontal cells. *Neuroscience* **6**, 679–688 (1981).
4. Silverman, S. M. & Wong, W. T. Microglia in the Retina: Roles in Development, Maturity, and Disease. *Annual Review of Vision Science* **4**, 45–77 (2018).
5. Wang, X. *et al.* Requirement for Microglia for the Maintenance of Synaptic Function and Integrity in the Mature Retina. *J. Neurosci.* **36**, 2827–2842 (2016).
6. Zhang, Y. *et al.* Repopulating retinal microglia restore endogenous organization and function under CX3CL1-CX3CR1 regulation. *Science Advances* **4**, eaap8492 (2018).
7. Joseph, A. *et al.* Imaging the dynamics of individual processes of microglia in the living retina in vivo. *Biomed. Opt. Express, BOE* **12**, 6157–6183 (2021).
8. Nimmerjahn, A., Kirchhoff, F. & Helmchen, F. Resting microglial cells are highly dynamic surveillants of brain parenchyma in vivo. *Science* **308**, 1314–1318 (2005).
9. Neumann, H., Kotter, M. R. & Franklin, R. J. M. Debris clearance by microglia: an essential link between degeneration and regeneration. *Brain* **132**, 288 (2009).
10. Zabel, M. K. *et al.* Microglial phagocytosis and activation underlying photoreceptor degeneration is regulated by CX3CL1-CX3CR1 signaling in a mouse model of retinitis pigmentosa. *Glia* **64**, 1479–1491 (2016).

690 11. Tremblay, M.-È. & Majewska, A. K. A role for microglia in synaptic plasticity? *Commun Integr*
691 *Biol* **4**, 220–222 (2011).
692 12. Sipe, G. O. *et al.* Microglial P2Y12 is necessary for synaptic plasticity in mouse visual cortex.
693 *Nat Commun* **7**, 10905 (2016).
694 13. Márquez-Ropero, M., Benito, E., Plaza-Zabala, A. & Sierra, A. Microglial Corpse Clearance:
695 Lessons From Macrophages. *Front Immunol* **11**, 506 (2020).
696 14. Karlen, S. J., Miller, E. B. & Burns, M. E. Microglia Activation and Inflammation During the
697 Death of Mammalian Photoreceptors. *Annual Review of Vision Science* **6**, 149–169 (2020).
698 15. Okunuki, Y. *et al.* Retinal microglia initiate neuroinflammation in ocular autoimmunity. *Proc*
699 *Natl Acad Sci U S A* **116**, 9989–9998 (2019).
700 16. Kremlev, S. G., Roberts, R. L. & Palmer, C. Differential expression of chemokines and
701 chemokine receptors during microglial activation and inhibition. *Journal of*
702 *Neuroimmunology* **149**, 1–9 (2004).
703 17. Babcock, A. A., Kuziel, W. A., Rivest, S. & Owens, T. Chemokine Expression by Glial Cells
704 Directs Leukocytes to Sites of Axonal Injury in the CNS. *J. Neurosci.* **23**, 7922–7930 (2003).
705 18. Boyce, M. *et al.* Microglia–Neutrophil Interactions Drive Dry AMD-like Pathology in a Mouse
706 Model. *Cells* **11**, 3535 (2022).
707 19. Zhou, H., Lapointe, B. M., Clark, S. R., Zbytnuik, L. & Kubes, P. A Requirement for Microglial
708 TLR4 in Leukocyte Recruitment into Brain in Response to Lipopolysaccharide. *The Journal of*
709 *Immunology* **177**, 8103–8110 (2006).
710 20. physiological_data_000664.pdf. https://www.jax.org/-/media/jaxweb/files/jax-mice-and-
711 services/physiological_data_000664.pdf (2007).

712 21. Burn, G. L., Foti, A., Marsman, G., Patel, D. F. & Zychlinsky, A. The Neutrophil. *Immunity* **54**,
713 1377–1391 (2021).
714 22. Peiseler, M. & Kubes, P. More friend than foe: the emerging role of neutrophils in tissue
715 repair. *J Clin Invest* **129**, 2629–2639 (2019).
716 23. Joseph, A., Chu, C. J., Feng, G., Dholakia, K. & Schallek, J. Label-free imaging of immune cell
717 dynamics in the living retina using adaptive optics. *eLife* **9**, e60547 (2020).
718 24. Sulai, Y. N., Scoles, D., Harvey, Z. & Dubra, A. Visualization of retinal vascular structure and
719 perfusion with a nonconfocal adaptive optics scanning light ophthalmoscope. *J Opt Soc Am*
720 *A Opt Image Sci Vis* **31**, 569–579 (2014).
721 25. Guevara-Torres, A., Williams, D. R. & Schallek, J. B. Origin of cell contrast in offset aperture
722 adaptive optics ophthalmoscopy. *Opt. Lett., OL* **45**, 840–843 (2020).
723 26. Chui, T. Y. P., VanNasdale, D. A. & Burns, S. A. The use of forward scatter to improve retinal
724 vascular imaging with an adaptive optics scanning laser ophthalmoscope. *Biomedical Optics*
725 *Express* **3**, 2537 (2012).
726 27. Guevara-Torres, A., Joseph, A. & Schallek, J. B. Label free measurement of retinal blood cell
727 flux, velocity, hematocrit and capillary width in the living mouse eye. *Biomed. Opt. Express,*
728 *BOE* **7**, 4228–4249 (2016).
729 28. Joseph, A. *et al.* Label-free tracking of single blood cells in the retinal immune response.
730 *Journal of Vision* **19**, 20–20 (2019).
731 29. Joseph, A., Guevara-Torres, A. & Schallek, J. Imaging single-cell blood flow in the smallest to
732 largest vessels in the living retina. *eLife* **8**, e45077 (2019).
733 30. Guevara-Torres, A., Williams, D. R. & Schallek, J. B. Imaging translucent cell bodies in the
734 living mouse retina without contrast agents. *Biomedical Optics Express* **6**, 2106 (2015).

735 31. Geng, Y. *et al.* Adaptive optics retinal imaging in the living mouse eye. *Biomed. Opt. Express*
736 **3**, 715–734 (2012).
737 32. Schallek, J., Geng, Y., Nguyen, H. & Williams, D. R. Morphology and topography of retinal
738 pericytes in the living mouse retina using in vivo adaptive optics imaging and ex vivo
739 characterization. *Invest. Ophthalmol. Vis. Sci.* **54**, 8237–8250 (2013).
740 33. Pinhas, A. *et al.* In vivo imaging of human retinal microvasculature using adaptive optics
741 scanning light ophthalmoscope fluorescein angiography. *Biomed Opt Express* **4**, 1305–1317
742 (2013).
743 34. Chu, C. J. *et al.* Multimodal analysis of ocular inflammation using the endotoxin-induced
744 uveitis mouse model. *Disease Models & Mechanisms* **9**, 473–481 (2016).
745 35. Hasenberg, A. *et al.* Catchup: a mouse model for imaging-based tracking and modulation of
746 neutrophil granulocytes. *Nat Methods* **12**, 445–452 (2015).
747 36. Crane, I. J. & Liversidge, J. Mechanisms of leukocyte migration across the blood–retina
748 barrier. *Semin Immunopathol* **30**, 165–177 (2008).
749 37. Xu, H. *et al.* Involvement of CD44 in leukocyte trafficking at the blood-retinal barrier. *Journal*
750 *of Leukocyte Biology* **72**, 1133–1141 (2002).
751 38. Xu, H. *et al.* Reduction in shear stress, activation of the endothelium, and leukocyte priming
752 are all required for leukocyte passage across the blood—retina barrier. *Journal of Leukocyte*
753 *Biology* **75**, 224–232 (2004).
754 39. Rosenbaum, J. T., McDevitt, H. O., Guss, R. B. & Egbert, P. R. Endotoxin-induced uveitis in
755 rats as a model for human disease. *Nature* **286**, 611–613 (1980).

40. Dubra, A. & Harvey, Z. Registration of 2D Images from Fast Scanning Ophthalmic Instruments. in *Biomedical Image Registration* (eds. Fischer, B., Dawant, B. M. & Lorenz, C.) 60–71 (Springer, Berlin, Heidelberg, 2010). doi:10.1007/978-3-642-14366-3_6.
41. Yang, Q. *et al.* Closed-loop optical stabilization and digital image registration in adaptive optics scanning light ophthalmoscopy. *Biomedical Optics Express* **5**, 3174 (2014).
42. Fiji: an open-source platform for biological-image analysis | Nature Methods. https://www.nature.com/articles/nmeth.2019.
43. Joseph, A., Guevara-Torres, A., Williams, D. R. & Schallek, J. B. Measurement of blood flow in the largest vessels and smallest capillaries in the living mouse retina using an adaptive optics scanning light ophthalmoscope. *Invest. Ophthalmol. Vis. Sci.* **56**, 3323–3323 (2015).
44. Dholakia, K., Guevara-Torres, A. & Schallek, J. B. Early changes in blood cell flux in retinal capillaries of diabetic and healthy mice imaged in vivo. *Invest. Ophthalmol. Vis. Sci.* **61**, 806–806 (2020).
45. Feng, G. *et al.* High-resolution structural and functional retinal imaging in the awake behaving mouse. *Commun Biol* **6**, 1–15 (2023).
46. Carter-Dawson, L. D. & LaVail, M. M. Rods and cones in the mouse retina. I. Structural analysis using light and electron microscopy. *J. Comp. Neurol* **188**, 245–262 (1979).
47. Jeon, C. J., Strettoi, E. & Masland, R. H. The major cell populations of the mouse retina. *J Neurosci* **18**, 8936–8946 (1998).
48. Dholakia, K. Y., Guevara-Torres, A., Feng, G., Power, D. & Schallek, J. In Vivo Capillary Structure and Blood Cell Flux in the Normal and Diabetic Mouse Eye. *Invest Ophthalmol Vis Sci* **63**, 18 (2022).

778 49. Wahl, D. J., Ng, R., Ju, M. J., Jian, Y. & Sarunic, M. V. Sensorless adaptive optics multimodal
779 en-face small animal retinal imaging. *Biomed Opt Express* **10**, 252–267 (2019).
780 50. Puthenparampil, M. *et al.* Hyper-Reflecting Foci in Multiple Sclerosis Retina Associate With
781 Macrophage/Microglia-Derived Cytokines in Cerebrospinal Fluid. *Front Immunol* **13**, 852183
782 (2022).
783 51. Pilotto, E. *et al.* Hyper-reflective retinal foci as possible in vivo imaging biomarker of
784 microglia activation in von Hippel-Lindau disease. *PLoS One* **17**, e0272318 (2022).
785 52. Kornmann, L. M. *et al.* Echogenic perfluorohexane-loaded macrophages adhere in vivo to
786 activated vascular endothelium in mice, an explorative study. *Cardiovasc Ultrasound* **13**, 1
787 (2015).
788 53. Paques, M. *et al.* Structural and hemodynamic analysis of the mouse retinal
789 microcirculation. *Invest. Ophthalmol. Vis. Sci* **44**, 4960–4967 (2003).
790 54. Stahl, A. *et al.* The Mouse Retina as an Angiogenesis Model. *Investigative Ophthalmology &*
791 *Visual Science* **51**, 2813–2826 (2010).
792 55. Senut, M.-C., Gulati-Leekha, A. & Goldman, D. An Element in the α1-Tubulin Promoter Is
793 Necessary for Retinal Expression during Optic Nerve Regeneration But Not after Eye Injury
794 in the Adult Zebrafish. *J. Neurosci.* **24**, 7663–7673 (2004).
795 56. Maidana, D. E., Gonzalez-Buendia, L., Miller, J. W. & Vavvas, D. G. Local photoreceptor cell
796 death differences in the murine model of retinal detachment. *Sci Rep* **11**, 18798 (2021).
797 57. Wan, J. *et al.* Preferential regeneration of photoreceptor from Müller glia after retinal
798 degeneration in adult rat. *Vision Research* **48**, 223–234 (2008).
799 58. Rösch, S. *et al.* The effects of iodoacetic acid on the mouse retina. *Graefes Arch Clin Exp*
800 *Ophthalmol* **253**, 25–35 (2015).

801 59. Nimmerjahn, A., Kirchhoff, F. & Helmchen, F. Resting microglial cells are highly dynamic
802 surveillants of brain parenchyma in vivo. *Science* **308**, 1314–1318 (2005).
803 60. Davalos, D. *et al.* ATP mediates rapid microglial response to local brain injury in vivo. *Nat*
804 *Neurosci* **8**, 752–758 (2005).
805 61. Shah, R. S., Soetikno, B. T., Lajko, M. & Fawzi, A. A. A Mouse Model for Laser-induced
806 Choroidal Neovascularization. *J Vis Exp* 53502 (2015) doi:10.3791/53502.
807 62. Khan, A. H. *et al.* A laser-induced mouse model of progressive retinal degeneration with
808 central sparing displays features of parafoveal geographic atrophy. *Sci Rep* **13**, 4194 (2023).
809 63. Strazzeri, J. M. *et al.* Focal damage to macaque photoreceptors produces persistent visual
810 loss. *Exp Eye Res* **119**, 88–96 (2014).
811 64. Dhakal, K. R. *et al.* Localized Photoreceptor Ablation Using Femtosecond Pulses Focused
812 With Adaptive Optics. *Transl Vis Sci Technol* **9**, 16 (2020).
813 65. Schwarz, C. *et al.* Selective S Cone Damage and Retinal Remodeling Following Intense
814 Ultrashort Pulse Laser Exposures in the Near-Infrared. *Investigative Ophthalmology & Visual*
815 *Science* **59**, 5973–5984 (2018).
816 66. Calford, M. B., Schmid, L. M. & Rosa, M. G. P. Monocular focal retinal lesions induce short–
817 term topographic plasticity in adult cat visual cortex. *Proceedings of the Royal Society of*
818 *London. Series B: Biological Sciences* **266**, 499–507 (1999).
819 67. Dreher, B., Burke, W. & Calford, M. B. Chapter 15 Cortical plasticity revealed by
820 circumscribed retinal lesions or artificial scotomas. in *Progress in Brain Research* vol. 134
821 217–246 (Elsevier, 2001).

822 68. Vitellas, C. *et al.* CONE PHOTORECEPTOR INTEGRITY ASSESSED WITH ADAPTIVE OPTICS
823 IMAGING AFTER LASER POINTER-INDUCED RETINAL INJURY. *Retinal Cases and Brief Reports*
824 **16**, 586 (2022).
825 69. Linton, E. *et al.* Retinal burns from laser pointers: a risk in children with behavioural
826 problems. *Eye* **33**, 492–504 (2019).
827 70. Current ROP Therapies: How Laser and Anti-VEGF Compare. *American Academy of*
828 *Ophthalmology* https://www.aao.org/eyenet/article/current-rop-therapies-how-laser-
829 antivegf-compare (2014).
830 71. Reddy, S. V. & Husain, D. Panretinal Photocoagulation: A Review of Complications. *Semin*
831 *Ophthalmol* **33**, 83–88 (2018).
832 72. Haupert, C. L. *et al.* Optimal laser power to rupture Bruch's membrane and the retinal vein
833 in the pig. *Ophthalmic Surg Lasers Imaging* **34**, 122–127 (2003).
834 73. Shah, R. S., Soetikno, B. T., Lajko, M. & Fawzi, A. A. A Mouse Model for Laser-induced
835 Choroidal Neovascularization. *J Vis Exp* e53502 (2015) doi:10.3791/53502.
836 74. Ley, K., Laudanna, C., Cybulsky, M. I. & Nourshargh, S. Getting to the site of inflammation:
837 the leukocyte adhesion cascade updated. *Nat Rev Immunol* **7**, 678–689 (2007).
838 75. Busch, E. M., Gorgels, T. G. & Van Norren, D. Filling-in after focal loss of photoreceptors in
839 rat retina. *Exp Eye Res* **68**, 485–492 (1999).
840 76. Lee, J. E., Liang, K. J., Fariss, R. N. & Wong, W. T. Ex vivo Dynamic Imaging of Retinal
841 Microglia using Time-lapse Confocal Microscopy. *Invest Ophthalmol Vis Sci* **49**, 4169–4176
842 (2008).
843 77. Jung, S. *et al.* Analysis of fractalkine receptor CX(3)CR1 function by targeted deletion and
844 green fluorescent protein reporter gene insertion. *Mol Cell Biol* **20**, 4106–4114 (2000).

845 78. Miller, E. B., Zhang, P., Ching, K., Pugh, E. N. & Burns, M. E. In vivo imaging reveals transient
846 microglia recruitment and functional recovery of photoreceptor signaling after injury.
847 *Proceedings of the National Academy of Sciences* **116**, 16603–16612 (2019).
848 79. Wu, C. Y. *et al.* Acute Solar Retinopathy Imaged With Adaptive Optics, Optical Coherence
849 Tomography Angiography, and En Face Optical Coherence Tomography. *JAMA*
850 *Ophthalmology* **136**, 82–85 (2018).
851 80. Allen, C. *et al.* Neutrophil Cerebrovascular Transmigration Triggers Rapid Neurotoxicity
852 through Release of Proteases Associated with Decondensed DNA. *The Journal of*
853 *Immunology* **189**, 381–392 (2012).
854 81. Panda-Jonas, S., Jonas, J. B. & Jakobczyk-Zmija, M. Retinal Photoreceptor Density Decreases
855 with Age. *Ophthalmology* **102**, 1853–1859 (1995).
856 82. Margalit, E. & Sadda, S. R. Retinal and Optic Nerve Diseases. *Artificial Organs* **27**, 963–974
857 (2003).
858 83. Sadik, C. D., Kim, N. D. & Luster, A. D. Neutrophils cascading their way to inflammation.
859 *Trends Immunol* **32**, 452–460 (2011).
860 84. Worthen, G. S. *et al.* Neutrophil-mediated pulmonary vascular injury. Synergistic effect of
861 trace amounts of lipopolysaccharide and neutrophil stimuli on vascular permeability and
862 neutrophil sequestration in the lung. *Am Rev Respir Dis* **136**, 19–28 (1987).
863 85. Linas, S. L., Whittenburg, D., Parsons, P. E. & Repine, J. E. Mild renal ischemia activates
864 primed neutrophils to cause acute renal failure. *Kidney Int* **42**, 610–616 (1992).
865 86. Uderhardt, S., Martins, A. J., Tsang, J. S., Lämmermann, T. & Germain, R. N. Resident
866 Macrophages Cloak Tissue Microlesions to Prevent Neutrophil-Driven Inflammatory
867 Damage. *Cell* **177**, 541-555.e17 (2019).

868 87. Pfeifer, C. W. *et al.* Dysregulated CD200-CD200R signaling in early diabetes modulates
869 microglia-mediated retinopathy. *Proceedings of the National Academy of Sciences* **120**,
870 e2308214120 (2023).
871 88. Miserocchi, E., Fogliato, G., Modorati, G. & Bandello, F. Review on the Worldwide
872 Epidemiology of Uveitis. *European Journal of Ophthalmology* **23**, 705–717 (2013).
873
874

Figures & videos:

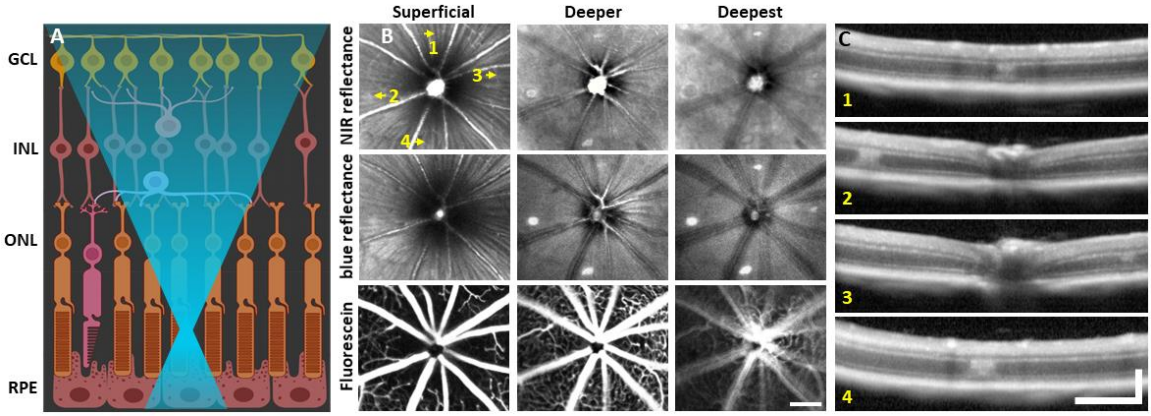

Figure 1. Laser injury assessed with commercial SLO and OCT. **(A)** 488 nm light is focused onto the photoreceptor outer segments using AOSLO. Created with Biorender.com. **(B)** 30° SLO images of NIR reflectance, blue reflectance and fluorescein angiography of a mouse retina 1 day after laser exposure. Three focal planes are shown. NIR and blue reflectance reveal small hyperreflective regions below the superficial plane. Fluorescein reveals intact vasculature with no sign of leakage. Arrows indicate regions with imparted laser damage (1-4). **(C)** OCT B-scans passing through laser-exposed regions indicated in B. Exposures produced a focal hyperreflective band within the ONL with adjacent retina appearing healthy. OCT images were spatially averaged (~30 µm, 3 B-scans). Scale bars = 200 µm horizontal, 200 µm vertical.

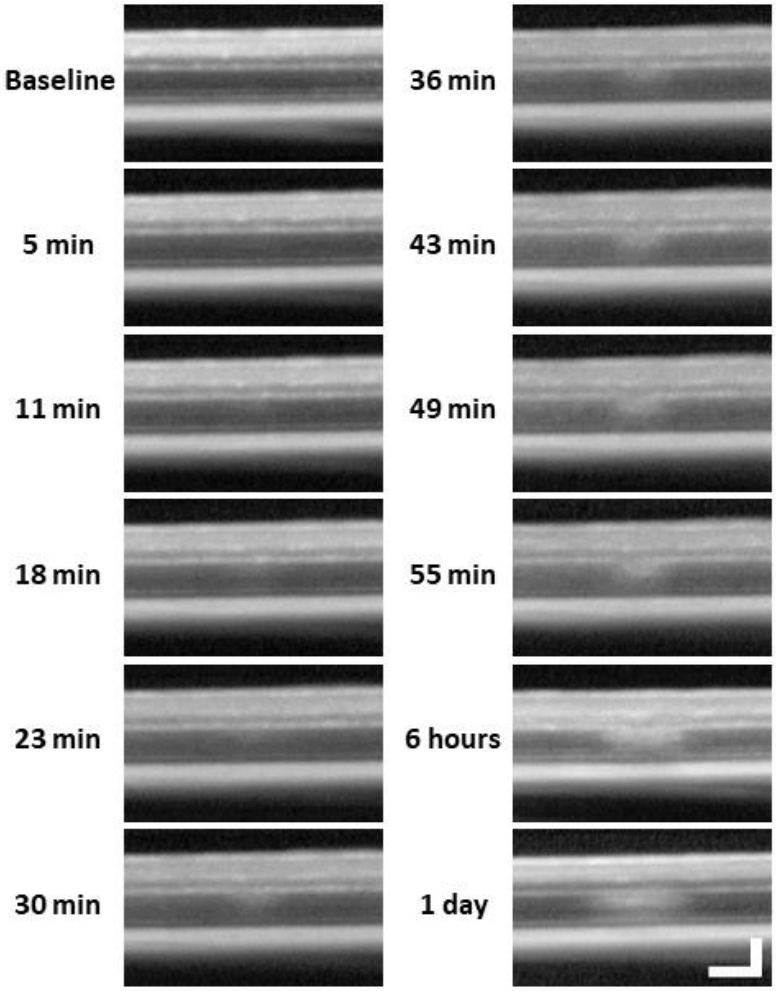

Figure 1 - figure supplement 1 Lesion location tracked from minutes to 1 day with OCT. After baseline OCT acquisition, OCT was performed every 5-7 minutes for one hour after 488 nm light exposure. 6 hour and 1 day time points were subsequently acquired. A band of hyperreflectivity forms near the OPL/ONL interface within 30 minutes of 488 nm light exposure. Hyperreflective band, spreads deeper into the ONL within ~1 hour. OCT images were spatially averaged (~30 µm, 8 B-scans). Scale bar = 40 µm horizontal, 100 µm vertical.

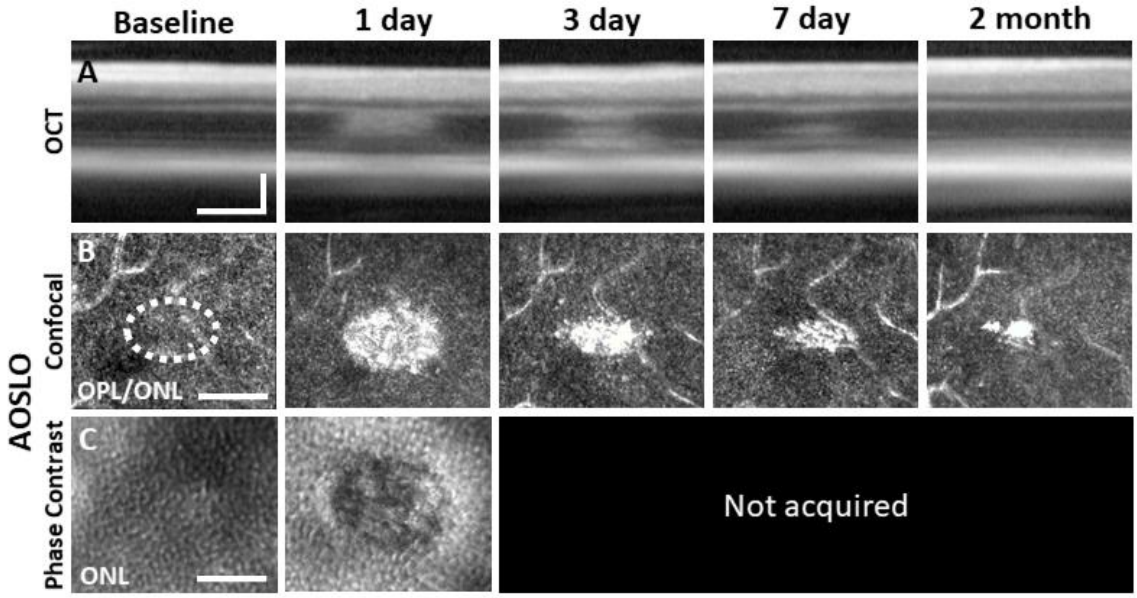

Figure 2. Laser damage temporally tracked with AOSLO and OCT. Laser-exposed retina was tracked with OCT **(A)**, confocal **(B)** and phase-contrast **(C)** AOSLO for baseline, 1, 3, 7 day and 2 month time points. OCT and confocal AOSLO display a hyperreflective phenotype that was largest/brightest at 1 day and became nearly invisible by 2 months. Dashed oval indicates region targeted for laser injury. Phase-contrast AOSLO revealed disrupted photoreceptor soma's 1 day after laser injury. Phase contrast data was not acquired for time points 3 days-2 months due to development of cataract which obscured the phase contrast signal. OCT images were spatially averaged (~30 µm, 8 B-scans). Scale bars = 40 µm, OCT image vertical scale bar = 100 µm.

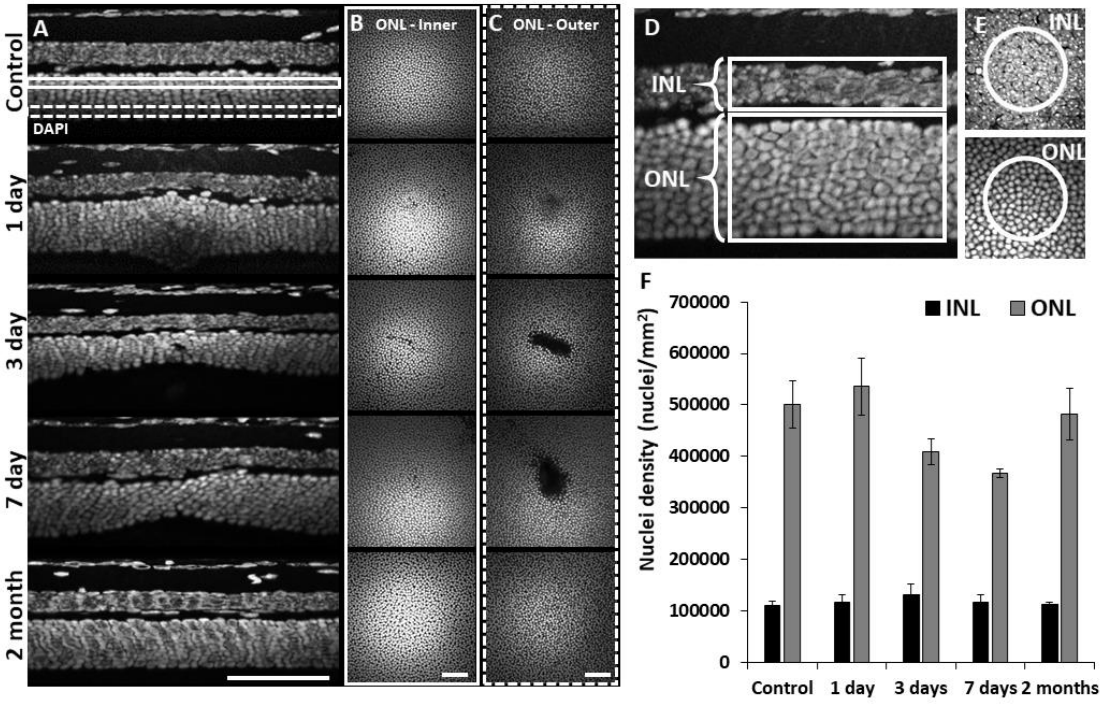

Figure 3. Retinal histology confirms photoreceptor ablation and preservation of inner retinal cells. Cross sectional view **(A)** and en-face **(B+C)** images of DAPI-stained whole-mount retinas (5 mice) at laser injury locations over time. By 1 day, ONL becomes thicker at lesion location, but thinner by 3 and 7 days. By 2 months, the ONL appeared similar to that of control. The inner (**B**, solid rectangle) and outer (**C**, dashed rectangle) stratum of ONL show axial differences in ONL loss**.** Most cell loss was seen in the outer aspect of the ONL **(C)**. Scale bars = 40 µm. **(D)** Cross section of DAPI-stained retina displaying INL and ONL regions for quantification. Each analysis region was 50 µm across and encompassed the entire INL or ONL. **(E)** En-face images show 50 µm diameter circles used for analysis. **(F)** Nuclei density for control and post-injury time points. ONL nuclei were reduced at 3 and 7 days ($p = 0.17$ and 0.07 respectively) while INL density remained stable ($n = 10$ mice, 3 unique regions per time point). Error bars display mean ± 1 SD.

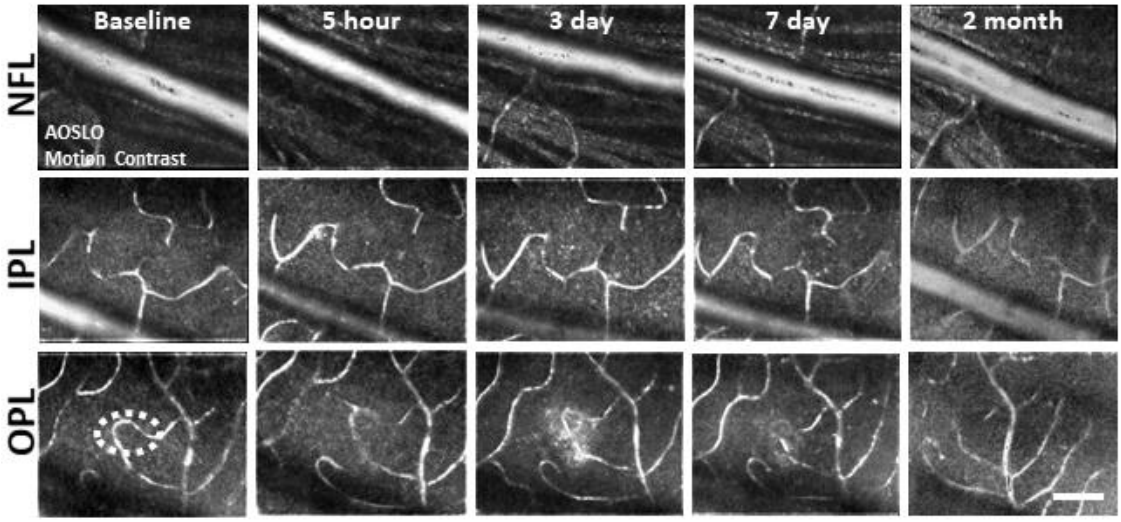

Figure 4. Microvascular perfusion unchanged after laser damage. A single location tracked over time and at three vascular plexuses using AOSLO. Motion-contrast images were generated from confocal videos to reveal vascular perfusion status. Retinal vasculature remained perfused for all time points tracked and at all depths. White oval indicates damage location. Scale bar = 40 µm.

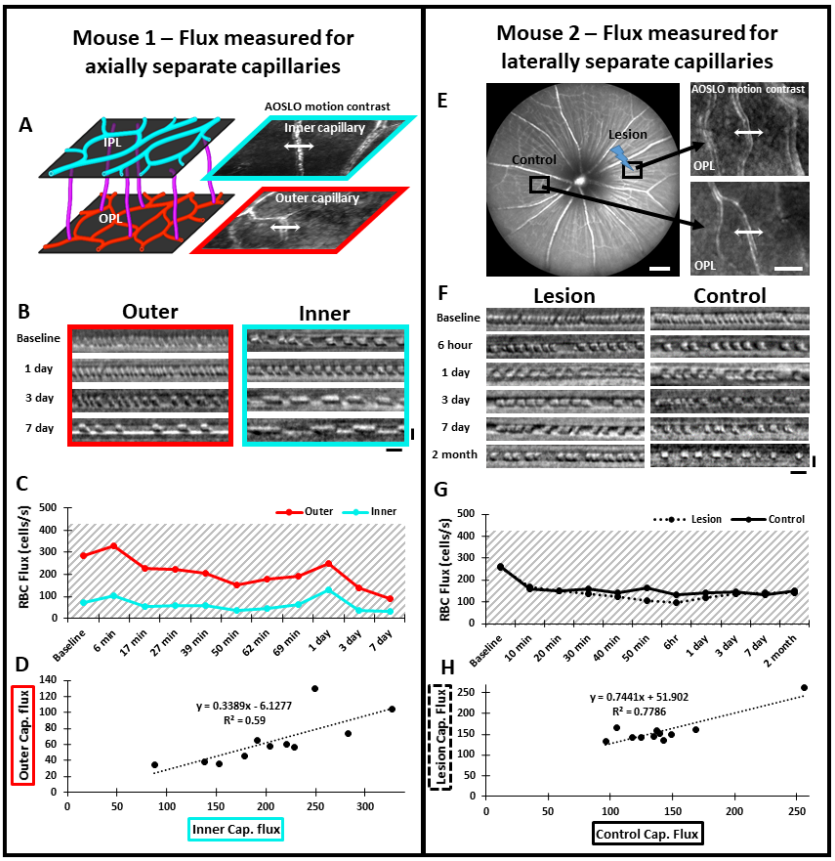

Figure 4 – figure supplement 1 Measurement of single-cell blood flux after laser damage using phase contrast AOSLO. **Mouse 1: (A)** The vascular plexus corresponding to IPL (cyan) and OPL (red) were targeted for flux determination. Blood cell flux was measured for 2 capillaries within the same field, at different depths. Arrows show the location for repeated line scan acquisitions. **(B)** RBC flux images were tracked up to 7 days post-damage. Scale bars = 10 ms, horizontal and 5 µm vertical. **(C)** Capillary flux measurements over 7 days. Despite the outer capillary displaying higher flux, both inner and outer capillaries changed synchronously for each time point. **(D)** Correlation of inner and outer capillary flux. Linear regression model displays a weak positive correlation (black dotted line). **Mouse 2: (E)** Left: Representative 55° SLO image showing regions targeted for capillary flux measurement. One region was subject to 488 nm laser damage and the other was left unlasered (Control). Scale bar = 200 µm. Right: Capillaries targeted for blood cell flux measurement. Arrows show the location for repeated line scan acquisitions. Scale bar = 40 µm. **(F)** RBC flux images were tracked up to 2 months post-damage. Scale bars = 10 ms horizontal and 5 µm vertical. **(G)** Capillary flux remained similar at lesion and control locations over all time points assessed. Gray shaded regions indicate range for normal capillary flux in the healthy C57BL/6J mouse (Dholakia et al 2022). **(H)** Correlation of flux in lesion and control locations. Linear regression model displays a positive correlation (black dotted line).

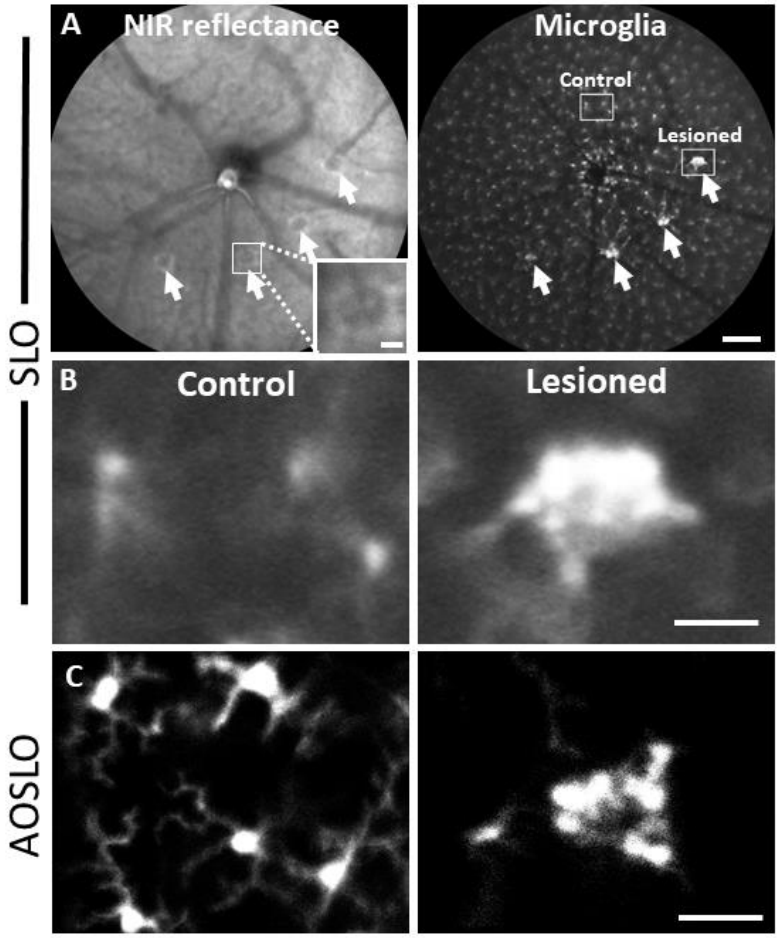

Figure 5. Microglial response 1 day after laser injury imaged in vivo with fluorescence SLO and AOSLO. **(A)** Left: Deep-focus NIR SLO fundus image (55˚ FOV) of laser-injured retina. White arrowheads point to damaged locations showing hyperreflective regions. Inset scale bar = 40 µm. Right: Fluorescence fundus image from same location. Fluorescent CX3CR1-GFP microglia are distributed across the retina and show congregations at laser-damaged locations. Scale bar = 200 µm. **(B)** Magnified SLO images of microglia at laser-damaged and control locations (indicated in A, right, white boxes). Control location displays distributed microglial whereas microglia at the lesion location are bright and focally aggregated. **(C)** Fluorescence AOSLO images show greater detail of cell morphology at the same scale. In control locations microglia showed ramified morphology and distributed concentration whereas damage locations revealed dense aggregation of many microglia that display less ramification. Scale bars = 40 µm.

Refer to .avi file

Figure 5 – video 1 Dynamic pseudopodia imaged with phase-contrast AOSLO 1 day post-injury. At the OPL/ONL border, a putative microglial pseudopod extension was captured among a field of static, disrupted PR somas. Video is 3 minutes elapsed. Scale bars = 20 μm.

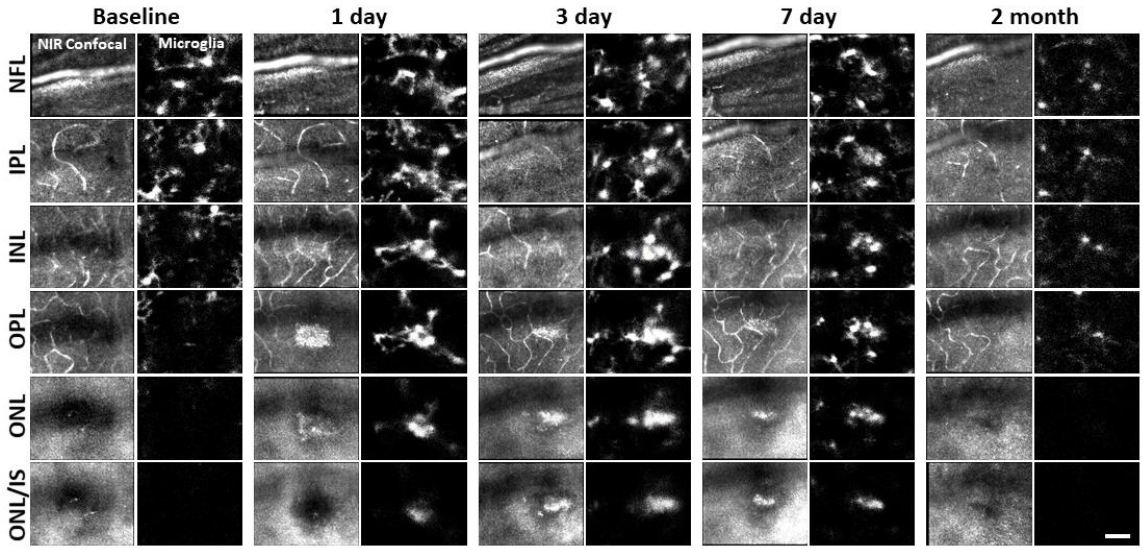

Figure 6. Microglial response to laser injury tracked with AOSLO. Simultaneously acquired NIR confocal and fluorescence AOSLO images across different retinal depths. Data are from one CX3CR1-GFP mouse tracked for 2 months. Microglia swarm to hyperreflective locations within 1 day. Microglia maintain an aggregated density for days and resolve by 2 months after damage. Scale bar = 40 µm.

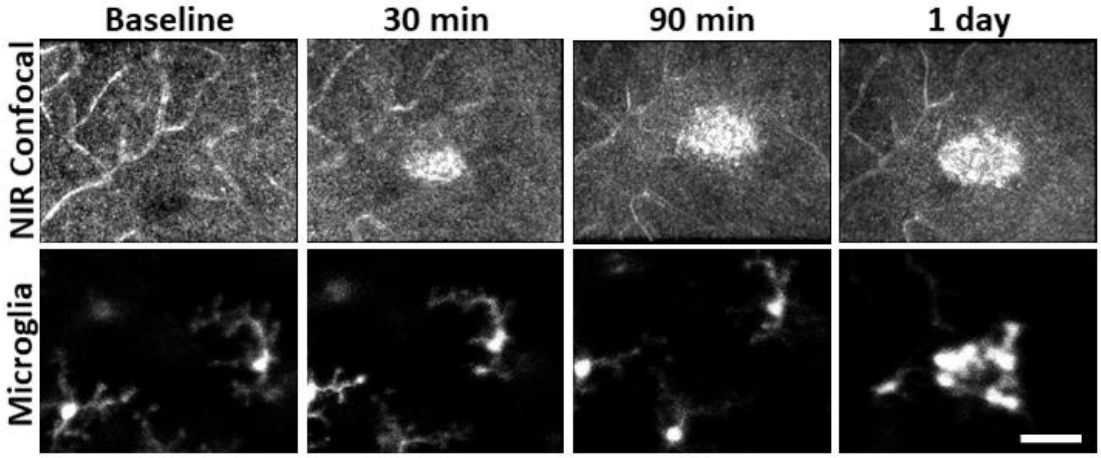

Figure 6 – figure supplement 1 Hyperreflective appearance emerges before microglia swarm to damage location. AOSLO confocal and fluorescence images were acquired for baseline, 30, 90 minute and 1 day post-laser exposure. The hyperreflective phenotype appeared within 30 minutes post damage. Microglia were not found to aggregate until ~1 day after. Scalebar = 40 μm.

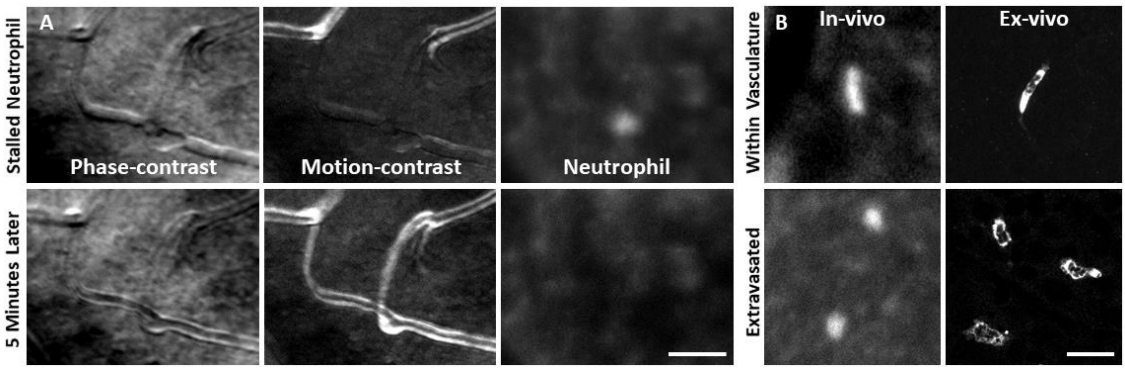

Figure 7. Neutrophil morphology imaged in vivo using AOSLO. **(A)** Phase-contrast, motion-contrast and fluorescence AOSLO reveal the impact of passing neutrophils on single capillaries. A rare and exemplary event shows a neutrophil transiently impeding capillary blood flow for minutes in healthy retina. Scale bar = 40 µm. **(B)** In-vivo AOSLO and ex-vivo fluorescence microscopy show neutrophils in two states. Neutrophils within capillaries displayed elongated, tubular morphology. Extravasated neutrophils were more spherical. Bottom images show extravasated neutrophils in response to LPS model for comparison (not laser damage model). Scale bar = 20 µm.

Refer to .avi file

Figure 7 – video 1 Neutrophil dynamics within a primary retinal vessel in a Catchup mouse. Confocal (left) and fluorescence (right) AOSLO were acquired from a large primary retinal vessel simultaneously. Several quickly flowing neutrophils are seen as streaks within the lumen of the large retinal vessel. Video plays in real-time (25 FPS, 20 seconds). Scale bar = 20 μm.

Refer to .avi file

Figure 7 – video 2 Neutrophils imaged in capillaries of a Catchup mouse. Motion-contrast (left) and fluorescence (right) AOSLO show a single neutrophil moving through a branch of the OPL capillary network. Red circles/arrows indicate neutrophil path within the vascular perfusion map. Rare neutrophils were found to move slowly through capillaries. Video is 0.4 seconds elapsed. Scale bar = 20 μm.

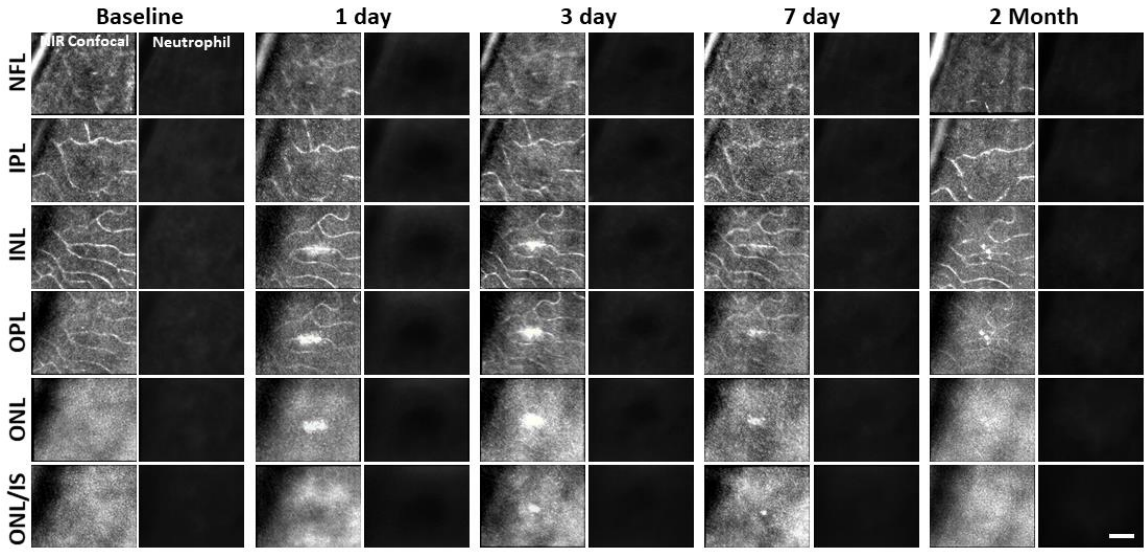

Figure 8. Retinal damage location tracked with AOSLO does not show accumulation of neutrophils. A single retinal location was tracked in a Catchup mouse from baseline to 2 months after lesion. Location of the lesion is apparent at 1 and 3 days post injury with diminishing visibility after 1 week. Despite the ability to detect neutrophils (Figure 7), we did not observe stalled, aggregated or an accumulation of neutrophils at any time point evaluated. This evaluation was confirmed at multiple depths ranging from the NFL to the ONL of the retina in vivo. Scale bar = 40 µm.

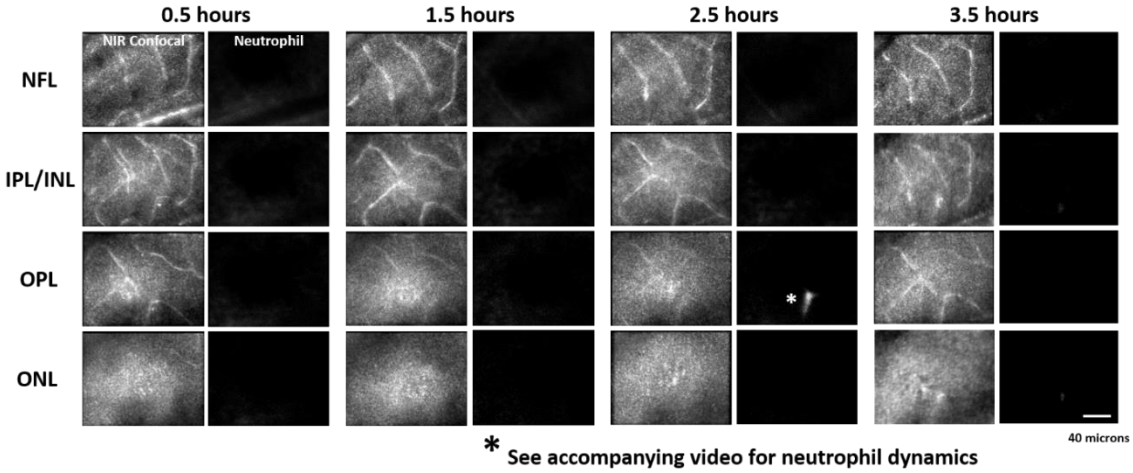

Figure 8 – figure supplement 1 A single mouse was tracked for 0.5 - 3.5 hours after a deep retinal lesion was placed at the center of the imaged field, adjacent to a large venule. Neutrophils did not extravasate within this early window post-lesion (also see figure 8 – video 3).

Refer to .avi file

Figure 8 – video 1 Neutrophil dynamics within a primary retinal vessel in a Catchup mouse 1 day after a deep retinal laser lesion is placed nearby. Confocal (left) and fluorescence (right) AOSLO images were acquired simultaneously. Quickly flowing neutrophils are seen as streaks within the lumen of this large retinal vessel and despite the adjacent deep retinal lesion (within 100 μm), there is no indication of rolling or crawling neutrophils. Video plays in real-time (25 FPS, 20 seconds). Scale bar = 20 μm.

Refer to .avi file

Figure 8 – video 2 Neutrophil dynamics within an OPL capillary in a Catchup mouse 1 day after deep laser injury. Motion-contrast (left) and fluorescence (right) AOSLO are displayed in tandem. At 1 day post-laser injury, a single neutrophil is seen moving through a capillary that runs directly through the injury site (yellow oval). Despite injury, neutrophil does not slow or stall at the lesion location. Video is 0.68 seconds elapsed. Scale bar = 20 μm.

Figure 8 – video 3 Neutrophil dynamics 2.5 hours post-lesion. Neutrophil movement indicates they stayed within OPL capillaries and did not extravasate into the retinal parenchyma at this early timepoint.

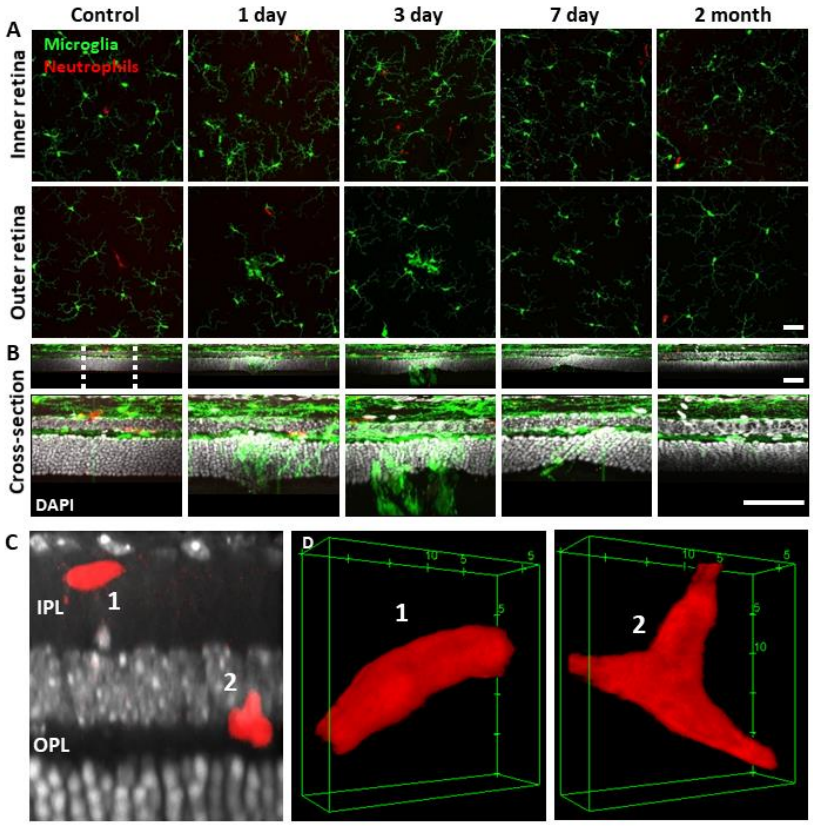

Figure 9. Neutrophil behavior under laser injury, as observed through ex vivo confocal microscopy, remains unresponsive despite marked microglial activation **(A)** En-face max intensity projection images of inner and outer (separated by approximate INL center) retinal microglia/neutrophils in Ly-6G-647-stained CX3CR1-GFP retinas. Microglia display focal aggregation in the outer retina for 1, 3 and 7 day time points that is resolved by 2 months. Neutrophils do not aggregate or colocalize to the injury location at any time point. Z-stacks were collected from 5 mice for the indicated time points. **(B)** Cross-sectional views of en-face z-stacks presented in A, including DAPI nuclear label. White dotted line indicates 100 µm region expanded below. Microglia migrate into the ONL by 1, 3 and 7 days post-laser injury and return to an axial distribution similar to that of control by 2 months. The few neutrophils detected remained within the inner retina. Scale bars = 40 µm. **(C)** Orthogonal view of DAPI-stained retina with Ly-6G-647-labelled overlay 1 day post-laser-injury. In a rare example, 2 neutrophils are found within the IPL/OPL layers despite a nearby outer retinal laser lesion. Scale bar = 20 µm. **(D)** Magnified 3D cubes representing cell 1 and 2 in C. Cell 1 displays pill-shaped morphology and cell 2 is localized to a putative capillary branch-point. Each are confined within vessels suggesting they do not extravasate in response to laser injury.

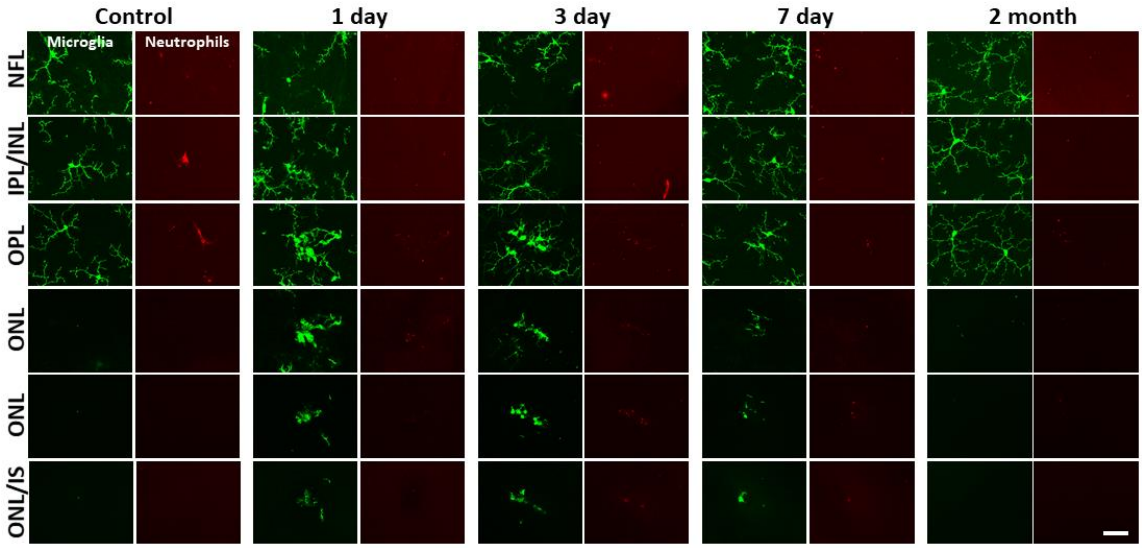

Figure 9 – figure supplement 1 Neutrophil/microglial response to laser injury tracked with *ex vivo* confocal microscopy. Simultaneously acquired GFP-positive microglia and Ly-6G-647-positive neutrophils were imaged with confocal microscopy in 5 CX3CR1-GFP mice. En-face images for several retinal depths are displayed. By 1, 3 and 7 days post-lesion, microglia have migrated into the outer retina, many appearing amoeboid and displaying fewer laterally-branching projections. Despite the deep microglial response, neutrophils stay within the inner retina and are not found in the avascular outer retinal layers. Scale bar = 40 µm.

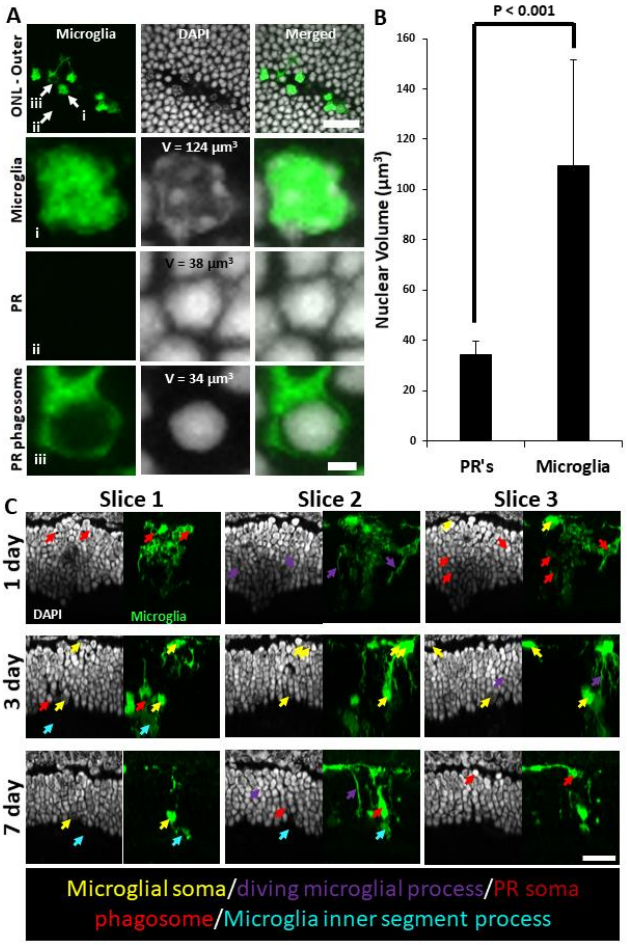

Figure 9 – figure supplement 2 Microglial PR phagosomes in the outer retina assessed with *ex vivo* confocal imaging. **(A)** En-face images of outer ONL in a DAPI-stained CX3CR1-GFP mouse 3 days post-laser-injury (top row). Microglia have infiltrated deep into the ONL and several PR phagosomes were identified. White arrows indicate locations for a single microglia (i), PR (ii) and PR phagosome (iii). These locations were expanded and displayed below. Microglia exhibited a heterogeneous nuclear staining pattern while PR nuclei exhibited homogenous DAPI fluorescence pattern. PR's displayed this pattern regardless of whether they were within a microglial phagosome or not. Top scale bar = 20 µm, bottom scale bar = 2 µm**. (B)** A finely-sliced (0.1 µm step size) outer retinal z-stack of DAPI-stained CX3CR1-GFP retina was used to quantify the average nuclear volume for infiltrated microglia (n = 14 nuclei) and PR's (n = 20 nuclei) for the same lesion site presented in A. On average, microglia had a statistically significant ($p < 0.001$) nuclear volume that was >3x that of PR's. These measurements allowed us to discriminate microglial somas from PR phagosomes. Error bars display mean + 1 SD. **(C)** Cross sections of DAPI-

stained outer retina in CX3CR1-GFP mice for 1, 3 and 7 days post-laser injury (n=3 mice). 3 representative planes (X-Z) through the lesion are displayed for each time point. Microglia form PR phagosomes within the ONL and microglial processes were seen extended into the PR inner/outer segment layer. Arrows label various morphological features seen at lesion sites: microglial somas (yellow), diving microglial process (violet), PR phagosome (red), microglial inner/outer segment process (cyan). Scale bar = 20 μm.

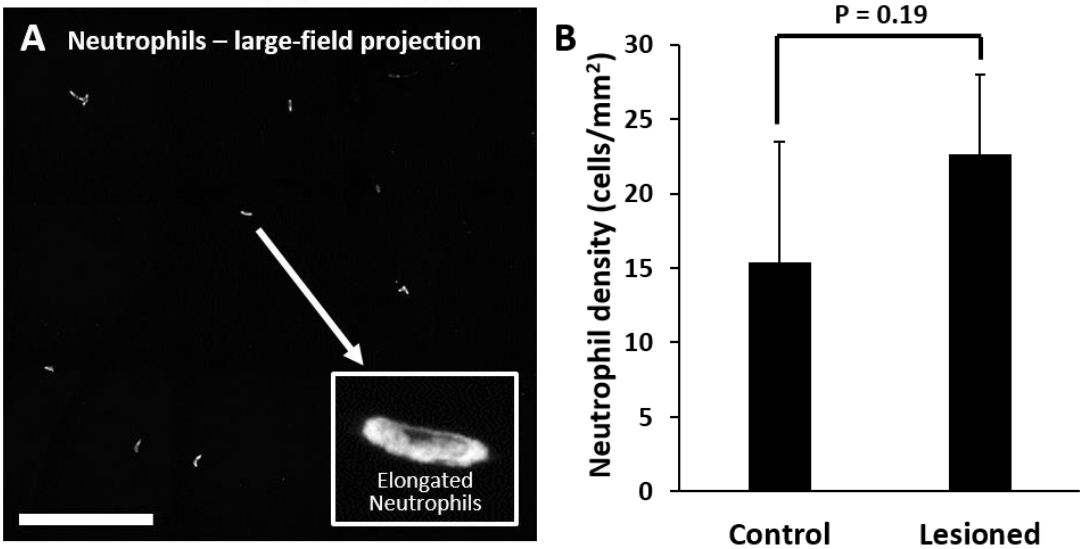

Figure 10. Quantification of neutrophils in laser damaged retinas assessed with ex vivo confocal microscopy over a wide-field. **(A)** Representative image displays neutrophils quantified using large-field (796 x 796 μm) z-stacks for control or 1 day after injury time points. In both control and laser injured retinas, neutrophils were sparse and confined to locations within capillaries suggesting they were the native fraction of circulating neutrophils at time of death. Inset displays expanded image of a single neutrophil. Scale bar = 200 μm. **(B)** Neutrophils quantified and displayed as the number of neutrophils per retinal area. The difference in number of neutrophils in control vs lesioned retinas was not statistically significant ($p = 0.19$). Error bars display mean + 1 SD.

Refer to .avi file

Video 1 Rotating 3D cubes of outer retinal nuclei and microglia after focal laser injury. Outer retinal Z-stacks of DAPI-stained whole-mount CX3CR1-GFP retinal tissue were imaged for control, 1, 3, 7 day and 2 month time points (n = 5 mice). DAPI + microglia composite cubes are displayed above and microglia cubes are displayed below. By 1 day, microglia send projections into the ONL, by 3 and 7 days, microglial somas have migrated into the ONL. Microglia within the ONL exhibit different morphology compared to the baseline condition. By 2 months, microglia are found back within the OPL, exhibiting lateral projections, similar to baseline. Scale bar = 40 μm.

Refer to .avi file

Video 2 Rotating 3D cubes of single neutrophils after laser injury or endotoxin induced uveitis. *Ex vivo* confocal z-stacks (0.1 μm steps) allowed detailed visualization of single neutrophils at 1 day after laser injury or 1 day after intravitreal LPS injection. After laser injury, neutrophils maintain a tubular, pill-shaped morphology (left). Occasionally, they would come to rest at capillary branch points (middle). In the EIU model, neutrophils extravasate into the retinal parenchyma and exhibit more spheroid morphology (right). We did not observe neutrophils to exhibit the extravasated morphology in response to laser injury.